Click Here for Full Article

Magnetohydrodynamic simulation of the interaction between two interplanetary magnetic clouds and its consequent geoeffectiveness

Ming Xiong,[1,2] Huinan Zheng,[1,2] S. T. Wu,[3] Yuming Wang,[1] and Shui Wang[1]

[1] Numerical studies of the interplanetary "multiple magnetic clouds (Multi-MC)" are performed by a 2.5-dimensional ideal magnetohydrodynamic (MHD) model in the heliospheric meridional plane. Both slow MC1 and fast MC2 are initially emerged along the heliospheric equator, one after another with different time intervals. The coupling of two MCs could be considered as the comprehensive interaction between two systems, each comprising of an MC body and its driven shock. The MC2-driven shock and MC2 body are successively involved into interaction with MC1 body. The momentum is transferred from MC2 to MC1. After the passage of MC2-driven shock front, magnetic field lines in MC1 medium previously compressed by MC2-driven shock are prevented from being restored by the MC2 body pushing. MC1 body undergoes the most violent compression from the ambient solar wind ahead, continuous penetration of MC2-driven shock through MC1 body, and persistent pushing of MC2 body at MC1 tail boundary. As the evolution proceeds, the MC1 body suffers from larger and larger compression, and its original vulnerable magnetic elasticity becomes stiffer and stiffer. So there exists a maximum compressibility of Multi-MC when the accumulated elasticity can balance the external compression. This cutoff limit of compressibility mainly decides the maximally available geoeffectiveness of Multi-MC because the geoeffectiveness enhancement of MCs interacting is ascribed to the compression. Particularly, the greatest geoeffectiveness is excited among all combinations of each MC helicity, if magnetic field lines in the interacting region of Multi-MC are all southward. Multi-MC completes its final evolutionary stage when the MC2-driven shock is merged with MC1-driven shock into a stronger compound shock. With respect to Multi-MC geoeffectiveness, the evolution stage is a dominant factor, whereas the collision intensity is a subordinate one. The magnetic elasticity, magnetic helicity of each MC, and compression between each other are the key physical factors for the formation, propagation, evolution, and resulting geoeffectiveness of interplanetary Multi-MC.

1. Introduction

[2] Space weather refers to the conditions on the Sun and in the solar wind, magnetosphere, ionosphere, and thermosphere that can influence the performance and reliability of space-borne and ground-based technological systems or can endanger human life or health, as defined in US National Space Weather Program Implementation Plan. A seamless forecasting system for space weather lies in the comprehensive and in-depth understanding of the Sun-Earth system. The never-stopping tremendous efforts have been made by humankind since the space age of the 1950s. A great deal of sophisticated observations beyond the Earth are now provided, with the launching of various spacecraft into deep space, such as Yohkoh, Geotail, Wind, SOHO, Ulysses, ACE, and TRACE in the 1990s and Cluster, RHESSI, SMEI, DS, Hinode (Solar B), and STEREO in the 21st century. These spacecraft missions construct an indispensable backbone in the establishment of space weather prediction system. Meanwhile, many models have been or are being developed and applied to space weather forecasting by utilizing most measurements of the above spacecraft, such as (1) HAF (Hakamada-Akasofu-Fry) [*Fry*

[1]Chinese Academy of Sciences Key Laboratory for Basic Plasma Physics, School of Earth and Space Sciences, University of Science and Technology of China, Anhui, China.
[2]State Key Laboratory of Space Weather, Chinese Academy of Sciences, Beijing, China.
[3]Center for Space Plasma and Aeronomic Research, University of Alabama in Huntsville, Huntsville, Alabama, USA.

et al., 2001, 2005]; (2) STOA (Shock Time of Arrival) [*Smart and Shea*, 1985]; (3) ISPM (Interplanetary Shock Propagation Model) [*Smith and Dryer*, 1990]; (4) an ensemble of HAF, STOA, and ISPM models [*Dryer et al.*, 2001, 2004; *McKenna-Lawlor et al.*, 2006]; (5) SPM (Shock Propagation Model) [*Feng and Zhao*, 2006]; (6) SWMF (Space Weather Modeling Framework) [*Toth et al.*, 2005]; (7) HHMS (Hybrid Heliospheric Modeling System) [*Detman et al.*, 2006]; (8) a data-driven Magneto-hydrodynamic (MHD) model of the University of Alabama in Huntsville [S. T. *Wu et al.*, 2005, 2006]; (9) a three-dimensional (3-D) regional combination MHD model with inputs of the source surface self-consistent structure based on the observations of the solar magnetic field and K-coronal brightness [*Shen et al.*, 2007]; (10) A merging model of SAIC MAS and ENLIL Heliospheric MHD Model [*Odstrcil et al.*, 2004b]; (11) an HAF + 3-D MHD model [*C.-C. Wu et al.*, 2005b, 2006b, 2007b, 2007c], and so on. However, great challenges are still faced to improve the prediction performance of space weather, as human civilization is relying more and more on space environment [*Baker*, 2002; *Fisher*, 2004].

[3]　The interplanetary (IP) space is a pivot node of the solar-terrestrial transport chain. Solar transients, for example, shocks and coronal mass ejections (CMEs), propagate in it, interact with it, and cause many consequences in the geospace. Magnetic clouds (MCs) are an important subset of interplanetary CMEs (ICMEs), occupying the fraction of nearly ∼100% (though with low statistics) at solar minimum and ∼15% at solar maximum [*Richardson and Cane*, 2004, 2005] and have significant geoeffectiveness [*Tsurutani et al.*, 1988; *Gosling et al.*, 1991; *Gonzalez et al.*, 1999; *Wu and Lepping*, 2002a, 2002b; *C.-C. Wu et al.*, 2003, 2006a; *Huttunen et al.*, 2005]. The current intense study of MCs could be traced back to the pioneer work by *Burlaga et al.* [1981], who first defined an MC with three distinct characteristics of enhanced magnetic field strength, smooth rotation of magnetic field vector, and low proton temperature and described it as a flux rope structure. An MC is widely thought to be the IP manifestation of a magnetic flux rope in the solar corona, which loses equilibrium and then escapes from the solar atmosphere into the IP space [*Forbes et al.*, 2006], with both ends still connecting to the solar surface [*Larson et al.*, 1997].

[4]　It is very likely for solar transients to interact with each other on their way to the Earth, especially at solar maximum when the daily occurrence rate of CMEs is about 4.3 in average on basis of the SOHO/Lasco CME catalogue (http://cdaw.gsfc.nasa.gov/CME_list). Some IP complicated structures were reported, such as complex ejecta [*Burlaga et al.*, 2002], multiple MCs (Multi-MC) [*Wang et al.*, 2002, 2003a], shock-penetrated MCs [*Wang et al.*, 2003b; *Berdichevsky et al.*, 2005; *Collier et al.*, 2007], non-pressure-balanced "MC boundary layer" associated with magnetic reconnection [*Wei et al.*, 2003a, 2003b, 2006], ICMEs compressed by a following high-speed stream [*Dal Lago et al.*, 2006], multiple shock interactions [*C.-C. Wu et al.*, 2005c, 2006c, 2007a]. However, all space-borne instruments, except the heliospheric imagers on board SMEI and STEREO, observe either the solar atmosphere within 30 solar radii by remote sensing, or the in situ space by local detecting, or both. Thus numerical simulations are necessary

to understand the whole IP dynamics. Below is an incomplete list of numerical studies of dynamical processes of CMEs/MCs and complex structures in the IP medium mentioned before: an individual CME/MC [*Vandas et al.*, 1995, 1996, 2002; *Groth et al.*, 2000; *Schmidt and Cargill*, 2003; *Odstrcil et al.*, 2003, 2004a, 2005; *Manchester et al.*, 2004; *C.-C. Wu et al.*, 2005a], the interaction of a shock wave with an MC [*Vandas et al.*, 1997; *Xiong et al.*, 2006a, 2006b], the interaction of multiple shocks [*C.-C. Wu et al.*, 2004a, 2004b, 2005c, 2006c, 2007a], and the interaction of multiple ejecta [*Gonzalez-Esparza et al.*, 2004; *Gonzalez-Esparza*, 2005; *Lugaz et al.*, 2005; *Xiong et al.*, 2005; *Y. M. Wang et al.*, 2004, 2005; *C.-C. Wu et al.*, 2006b, 2007c; *Hayashi et al.*, 2006]. Therein, *C.-C. Wu et al.* [2005c, 2006c, 2007a] performed a 1.5-D MHD model to simulate the famous Halloween 2003 epoch, in which eruption time of solar flares was used as input timing for solar disturbances to study the shock-shock interaction (and overtaking) and the matching of shock arrival time at 1 AU with observations (ACE). In addition, *C.-C. Wu et al.* [2006b, 2007c] performed 3-D global simulations by combining two simulation models (HAF + 3-D MHD) to study the interacting and overtaking of two ICMEs. These observation and simulation efforts do advance our understanding of solar-terrestrial physics.

[5]　The Multi-MCs have already been verified by observations to be an important IP origin for the great geomagnetic storms [*Wang et al.*, 2002, 2003a; *Xue et al.*, 2005; *Farrugia et al.*, 2006; *Xie et al.*, 2006; *Zhang et al.*, 2007]. Particularly for the eight extremely large geomagnetic storms with $Dst \leq -200$ nT during the year 2000 ∼ 2001, two of them were caused by Multi-MCs and one caused by shock-MC interacting structure [*Xue et al.*, 2005]. Most recently, via summarizing the efforts of the NASA Living With a Star (LWS) Coordinated Data Analysis Workshop (CDAW) held at George Mason University in March 2005, *Zhang et al.* [2007] proposed that 24 out of 88 (27%) major geomagnetic storms with $Dst \leq -100$ nT from the year 1996 to 2005 were produced by multiple interacting ICMEs arising from multiple halo CMEs launched from the Sun in a short period. So the Multi-MC plays a notable role in producing large geomagnetic storms. There are two possible conditions for double-MC formation [*Wang et al.*, 2004]: (1) The speed of following MC should be faster than that of preceding MC; (2) The separation between the eruption of two MCs should be moderate (about 12 h based on statistics of observed events). Evolutionary signatures of ICMEs interacting are found from spacecraft observations, that is, heating of the plasma, acceleration/deceleration of the leading/trailing ejecta, compressed field and plasma in the leading ejecta, possible disappearance of shocks, and strengthening of the shock driven by the accelerated ejecta [*Farrugia and Berdichevsky*, 2004]. Previous simulations of interaction between two magnetic flux ropes in the IP space [*Lugaz et al.*, 2005; *Y. M. Wang et al.*, 2005], the solar corona [*Schmidt and Cargill*, 2004; *A. H. Wang et al.*, 2005; *Lugaz et al.*, 2007], and a local homogeneous medium background [*Odstrcil et al.*, 2003] only address a few typical cases in the dynamical aspect. Here a comprehensive study of many cases of MCs interacting under various conditions is carried out for better understanding of both dynamics and ensuing

Table 1. Assortment of Simulation Cases of Individual MC

Group	Case	v_{mc}, 10^2 km/s	Comment
IM_1	b_1, c_1, d_1, e_1, f_1, g_1, h_1, i_1, j_1	4, 6, 5, 7, 8, 9, 10, 11, 12	individual MC ($H_{mc} = 1$)
IM_2	b_2, c_2, d_2, e_2, f_2, g_2, h_2, i_2, j_2	4, 6, 5, 7, 8, 9, 10, 11, 12	individual MC ($H_{mc} = -1$)

geoeffectiveness. The interaction between two systems, each composed of an MC and its driven shock, could be considered in some senses as a generalization of our recent studies of MC-shock interaction [*Xiong et al.*, 2006a, 2006b]. Thus we address the following two issues naturally: (1) What is the role of the following MC body in Multi-MC evolution in comparison with our previous studies [*Xiong et al.*, 2006a, 2006b] of MC-shock interaction? (2) At what evolutionary stage a Multi-MC at 1 AU reaches the maximum geoeffectiveness? The above answers are explored by a 2.5-D numerical model in ideal MHD process.

[6] The force-free magnetic flux rope models have been proven to be very valuable to interpret in situ observations of MCs [e.g., *Lundquist*, 1950; *Burlaga*, 1988; *Farrugia et al.*, 1993; *Chen*, 1996; *Owens et al.*, 2006]. Particularly, Lundquist model [*Lundquist*, 1950] is adopted in our model to describe the magnetic field configuration of an MC, as widely applied in the space science literature [e.g., *Vandas et al.*, 1995, 1996; *Y. M. Wang et al.*, 2002, 2003d, 2005; *Xiong et al.*, 2006a, 2006b]. A following fast MC overtaking and interacting a preceding slow one in the IP space could result in a Multi-MC structure [*Wang et al.*, 2002, 2003a]. In order to explore the basic physics process of Multi-MC, we make the following assumptions to simplify the complex circumstance of double-MC structure in the numerical MHD simulation: (1) two MCs' axes parallel or antiparallel with each other; (2) their axes are both within the ecliptic plane and perpendicular to the Sun-Earth line; (3) each MC is symmetric in the azimuth direction of the heliosphere and considered as an ideal loop encompassing the Sun; (4) magnetic reconnection does not exist in double MC interacting; (5) both MCs have the same size, mass, magnetic field strength, and plasma β. Thus two MCs in our model only differ in magnetic helicity sign H_{mc} and initial radial liftoff speed v_{mc}. A parametric study of H_{mc} and v_{mc} is focused in our model for the very specialized Multi-MC structure. Since the two MCs are very alike except H_{mc} and v_{mc}, they could be, to some extent, considered to be identical. MC1 and MC2 are used to label the two MCs launched from the Sun, one after another, respectively. Because an MC boundary is a self-enclosed magnetic surface and two MCs' magnetic field lines would not blend under the condition of the strictly ideal MHD process, the substructures of double MCs, corresponding to the previously separated MC1 and MC2 before collision, could be easily differentiated and accordingly named as sub-MC1 and sub-MC2.

[7] The goal of the present work is to conduct a systematic investigation of Multi-MC in the IP space. We give a brief description of the numerical MHD model in section 2, describe the dynamical behavior of MC-MC interaction in

section 3, discuss the consequent geoeffectiveness in section 4, analyze the compressibility of MC-MC collision in section 5, and summarize the paper in section 6.

2. Numerical MHD Model

[8] The Multi-MC simulation is accommodated by a few slight modifications from our previous numerical model for MC-shock interaction [*Xiong et al.*, 2006a, 2006b]. These modifications are as follows: (1) The top boundary of simulated domain is extended from 300 to 400 R_s; (2) The following shock is replaced by a following MC; (3) The initial speed v_{mc}, emergence time t_{mc}, and magnetic helicity H_{mc} out of all input parameters for each sub-MC of Multi-MC are independently selected to make various combinations for parametric study shown in Table 2. First, the propagation through the IP space is modeled by numerical simulation. Then, the geomagnetic storm excited by the solar wind-magnetosphere-ionosphere coupling is approximated by an empirical formula of Burton $\frac{dDst(t)}{dt} = Q(t) - \frac{Dst(t)}{\tau}$ [*Burton et al.*, 1975]. Here the coupling function $Q = v_r \operatorname{Min}(B_z, 0)$ and the diffusion timescale $\tau = 8$ h, with the radial solar wind speed and south-north magnetic field component, respectively, denoted by v_r and B_z. Burton model [*Burton et al.*, 1975] for geomagnetic disturbance has been analyzed and validated [*Wang et al.*, 2003d; *Wang*, 2003], and applied in Dst evaluation [*Wang et al.*, 2003d; *Wang*, 2003; *Xiong et al.*, 2006a, 2006b]. Thus the physical process of cause-effect transport chain for solar disturbances is fully described in our model. Moreover, the MC2-driven shock in all of our simulation cases is faster than the local magnetosonic speed all the way and strong enough so that it would not be dissipated in the low β MC1 medium [*Xiong et al.*, 2006a, 2006b].

3. MC1-MC2 Interaction

[9] All 48 simulation cases of MC1-MC2 coupling are assorted into four groups in Table 2, with 18 cases of individual MC in two groups of Table 1 for comparison. Here, IM, EID, and CID stand for "Indiviual MC," "Eruption Interval Dependence," and "Collision Intensity Dependence," respectively, with the subscripts 1 and 2 denoting the sign of magnetic helicity. Case C_1 is shared by Groups EID_1 and CID_1 and Case C_2 by Groups EID_2 and CID_2. In our simulation, an MC with southward/northward magnetic field in its rear half is defined to have positive/negative helicity. Both MCs are associated with positive helicities in groups EID_1 and CID_1, meanwhile MC1 and MC2 are respectively associated with positive and negative helicities in groups EID_2 and CID_2.

[10] The numerical simulation is performed in the ideal MHD process. The artificial numerical magnetic reconnection between MCs is strictly ruled out by a specific numerical technique [cf. *Hu et al.*, 2003]. Thus the dynamics in groups IM_1, EID_1, and CID_1 is nearly the same as that in groups IM_2, EID_2, and CID_2, respectively, whereas the geoeffectiveness is highly different due to the reversed north and south magnetic components within the cloud with opposite helicity. Moreover, by changing Dt ($Dt = t_{mc2} - t_{mc1}$, $t_{mc1} = 0$ h), the initiation delay between a preceding MC of 400 km/s and a following MC of 600 km/s in groups

EID$_1$ and EID$_2$, the Multi-MC formed by the MC1 and MC2 may reach different evolutionary stages on its arrival at 1 AU. Therefore the eruption interval dependence for MC1-MC2 interaction is easily discriminated by a comparative study. Similarly, collision intensity dependence is also explored by a parametric study of v_{mc2} from 450 to 1200 km/s in groups CID$_1$ and CID$_2$. Meanwhile the full interaction between subclouds within 1 AU to maximally highlight collision effect is guaranteed by t_{mc2} = 12.2 h in groups CID$_1$ and CID$_2$. Furthermore, an individual MC with its speed from 400 to 1200 km/s in groups IM$_1$ and IM$_2$ supplements indispensably to other groups for the study of coupling effect of two MCs. Cases B$_1$ and B$_2$ with t_{mc2} = 30.1 h, C$_1$ and C$_2$ with t_{mc2} = 12.2 h, are typical examples of Multi-MC in the early and late evolutionary stages, respectively, which are addressed below in details.

3.1. Case B$_1$

[11] In Case B$_1$, we discuss the results of MC1-MC2 interaction for eruption speed v_{mc1} = 400 km/s, v_{mc2} = 600 km/s, and initiation delay t_{mc2} = 30.1 h. Figure 1 shows the successive behavior of MC1-MC2 interaction of Case B$_1$. The magnetic field lines, among which two are enclosed white solid lines marking the boundaries of MC1 and MC2, respectively, are superimposed on each color-filled contour image, and two radial profiles, one through the equator (noted by Lat. = 0°), the other through 4.5° southward (white dashed lines in the images, noted by Lat. = 4.5°S), are plotted below. One can read the global vision from the images and local details from the profiles simultaneously for the propagation and evolution of Multi-MC. For better highlighting the local disturbance, Figures 1a–1c show the magnitude B of magnetic field from which the initial value $B|_{t=0}$ is deducted. Two identical MCs are successively injected into the IP space with different initial eruption speed. As long as the fast following MC2 lags behind the slow preceding MC1, each of them behaves as an individual event, and satisfies the criteria of a single MC. Because the MC-driven shock and incidental shock [Xiong et al., 2006a] both propagate along the heliospheric current sheet (HCS) in the IP medium, their inherent traits are identically characterized by a concave-outward morphology with the position of the strongest intensity being roughly 4.5° away from the HCS. MC2-driven shock just approaches MC1 body tail at 46.5 h, as seen from Figure 1d. Across this shock front, radial speed v_r increases abruptly from 440 km/s at MC1 tail to 670 km/s at MC2 head. From then on, MC2 and MC1 will directly collide to form a special IP complex named Multi-MC by Wang et al. [2002, 2003a], and their evolution will be coupled with each other. Consequently, the characteristic parameters of each sub-MC would change drastically due to the nonlinear interaction. At 56.1 h, MC2-driven shock front has already entered MC1 body across which radial speed v_r abruptly jumps from 445 to 620 km/s, but MC2 body is still unable to catch up with

MC1 tail (Figure 1e) because of t_{mc2} = 30.1 h. The dynamic response of Multi-MC at this snapshot is merely ascribed to the interaction between MC2-driven shock and MC1 body. So the preceding MC1 behavior in Figures 1b, 1e and 1h are similar to its counterpart of MC-shock interaction in essence [cf. Xiong et al., 2006a, Figures 3c, 3f, and 3i]. Large compression within MC1 medium downstream of MC2-driven shock front is very pronounced from an abnormal local spike-like structure of c_f along Lat. = 4.5°S, as shown in Figure 1h. The orientation of magnetic field lines is also rotated in MC1 medium swept by the shock front. As the shock continuously advances into MC1 body, the morphology of MC1 rear part is transformed from an original rough semicircle (Figure 1d) to a V-shape with a wide open mouth (Figure 1f). Moreover MC2 body has already contacted MC1 tail at the bottom of so-called V shape along the equator at 80.7 h, when the MC2-driven shock cannibalizes the rear half of MC1 body (Figure 1f). Since then, MC2 body is directly involved into interaction with MC1 body. The Multi-MC evolution has reached a new critical stage, for MC1 will undergo the most violent compression from the ambient solar wind ahead, continuous penetration of MC2-driven shock through MC1 body, and persistent pushing of MC2 body at MC1 tail boundary. In Figure 1f, nearly constant speed in MC1 rear half and large speed difference with 80 km/s across MC1 rear boundary along the equator imply continuous strike of high-speed MC2 body upon preceding MC1 body. Besides, the interplanetary magnetic field (IMF) within Multi-MC envelope is highly bending just behind MC2-driven shock front (Figures 1c, 1f, and 1i), as a result of rotation across the shock front and draping around either subcloud surface.

[12] The in situ observation along Lat. = 4.5°S by a hypothetical spacecraft at Lagrangian point (L1) is illustrated in Figure 2. With each sub-MC boundary identified as dashed lines, the MC1 duration of 18 h is much less than MC2 duration of 26 h due to the compression in MC1 rear half accompanying with MC2-driven shock advancing. The MC2 "senses" the existence of preceding MC1, though its response is much less sensitive. The location of maximum bulk flow speed v_r in MC2 body is shifted by 6 h later (Figure 2c) from MC2 head [cf. Xiong et al., 2006a, Figure 2], between which magnitude B is obviously enhanced (Figure 2a). The dawn-dusk electric field VB_z is calculated by the product of v_r and B_θ in the spherical geometry of this simulation. Beginning from 74 h, VB_z, negative in MC1 rear half, positive in MC2 front half, and negative again in MC2 rear half (Figure 2d), is responsible for Dst dropping from 0 nT at 74 h to −140 nT at 82 h, recovering from −140 nT at 82 h to −25 nT at 97 h, and dropping again from −25 nT at 97 h to −75 nT at 114 h, respectively (Figure 2e). Owing to compression of southward magnetic component B_s (B_s = Min(B_θ, 0)) within MC1 rear part, the first Dst dip with −140 nT is much lower than the second one with −75 nT for geomagnetic storm.

Figure 1. Evolution of MC2 overtaking MC1 for Case B$_1$, with (a)–(c) magnetic field magnitude B, (d)–(f) radial flow speed v_r, and (g)–(i) radial characteristic speed of fast mode c_f. Attached below each image are two additional radial profiles along Lat. = 0° and 4.5°S. Note that radial profile of B is plotted by subtracting the initial ambient value $B|_{t=0}$. The white solid line in each image denotes the MC boundary. Solid and dashed lines at each profile denote MC core and boundary. Only part of domain is adaptively plotted to highlight Multi-MC.
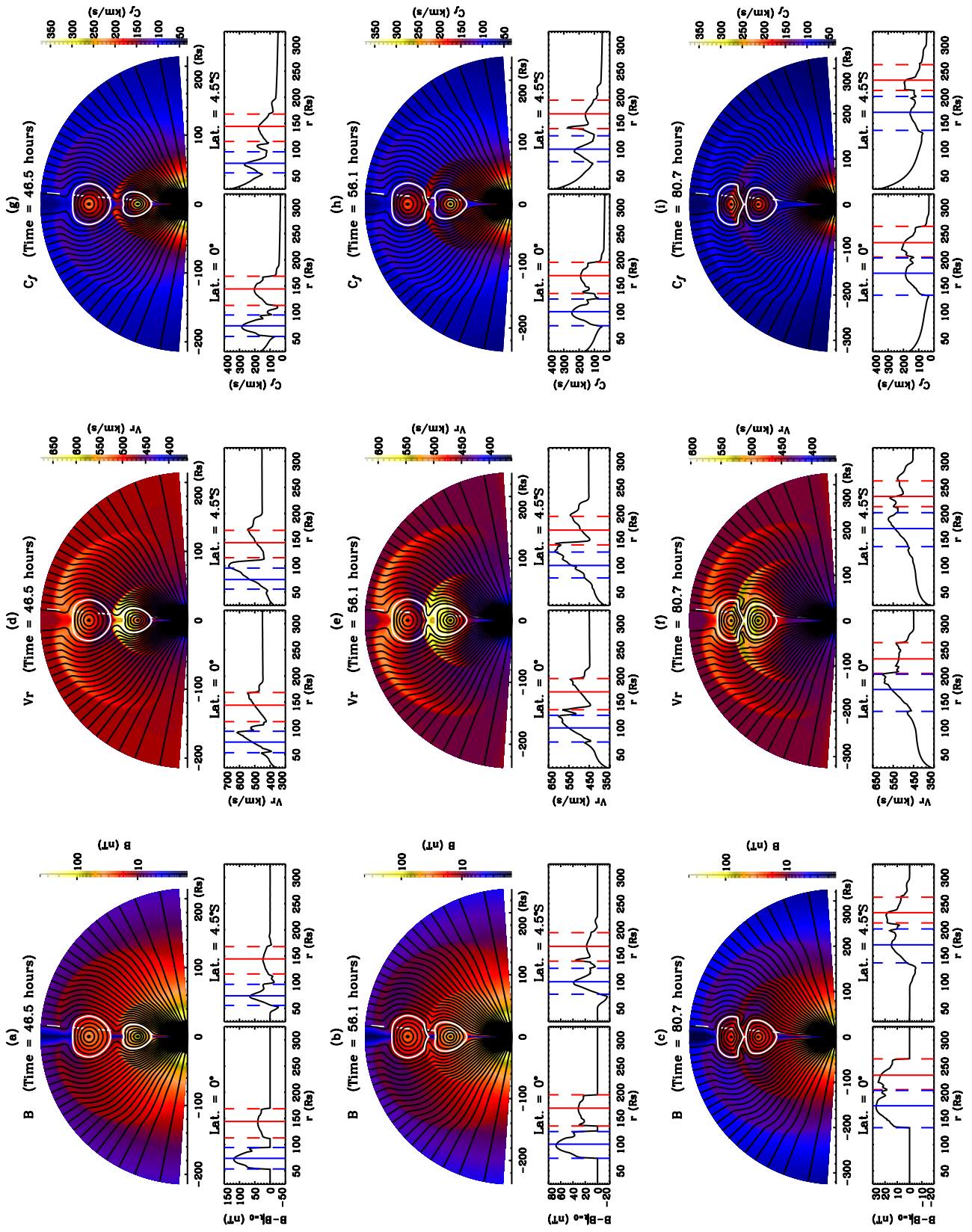
Figure 1
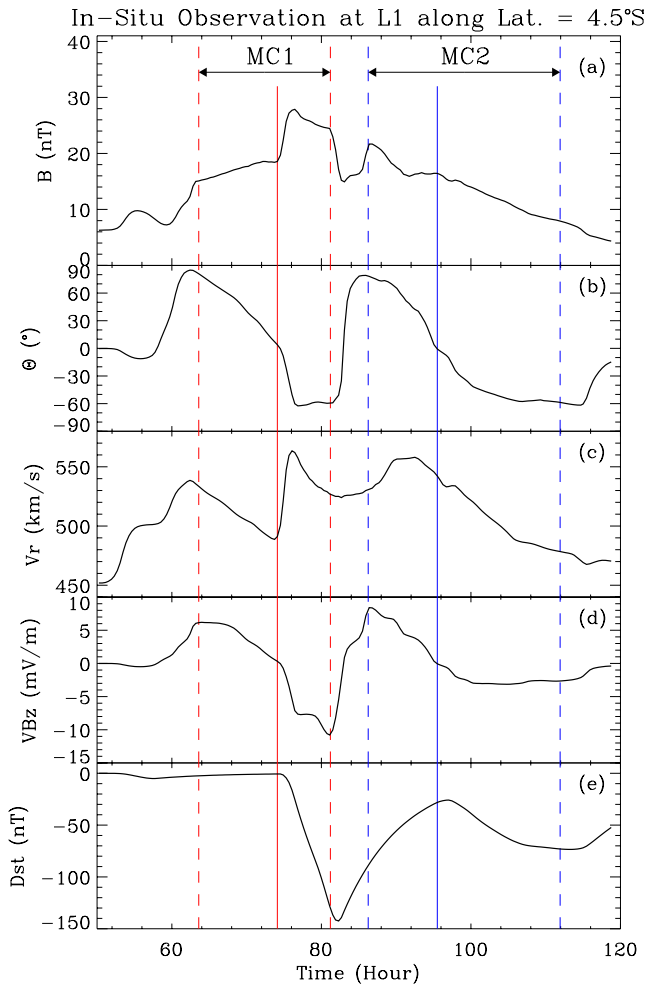
Figure 2. In situ hypothetical observation along Lat. = 4.5°S for Case B_1. Stacked from top to bottom are (a) magnetic field magnitude B, (b) elevation of magnetic field Θ, (c) radial flow speed v_r, (d) derived dawn-dusk electric field VB_z, and (e) Dst index. Solid and dashed delimiting lines denote MC center and boundary.

Particularly, the two Dst dips are separated by only 32 h because the geoeffectiveness of two IP triggers (MC1 and MC2) are superposed together. The idea of a two-ejecta event associated with a two-step geomagnetic storm was recently proposed and verified by *Farrugia et al.* [2006] on basis of observation. Hence the association of two Dst dips lies in the MC1-MC2 interaction.

3.2. Case C_1

[13] In order to realize the fully interaction between MC1 and MC2 before their arrival at L1, t_{mc2}, the emergence time of MC2, is scheduled earlier to be 12.2 h with both MCs having the same speeds of Case B_1. Only the evolution of v_r is given in Figure 3 to visualize multicloud structure. Comparing to that in Figures 1c, 1f and 1i, the so-called "V-shape" morphology of MC1 rear half becomes very flat under the pounding of very high-speed MC2 body at 19.5 h as Multi-MC evolution proceeds, as shown in Figure 3a. As a result, contact position between MC1 and MC2 body is extended from one single point at the HCS (Figure 1f) to a

straight line between Lat. = 4.5°S and 4.5°N (Figure 3a). The MC1's magnetic elasticity seems to be too vulnerable to resist the violent collision from MC2 body. The collision efficiently transfers the radial momentum from the fast
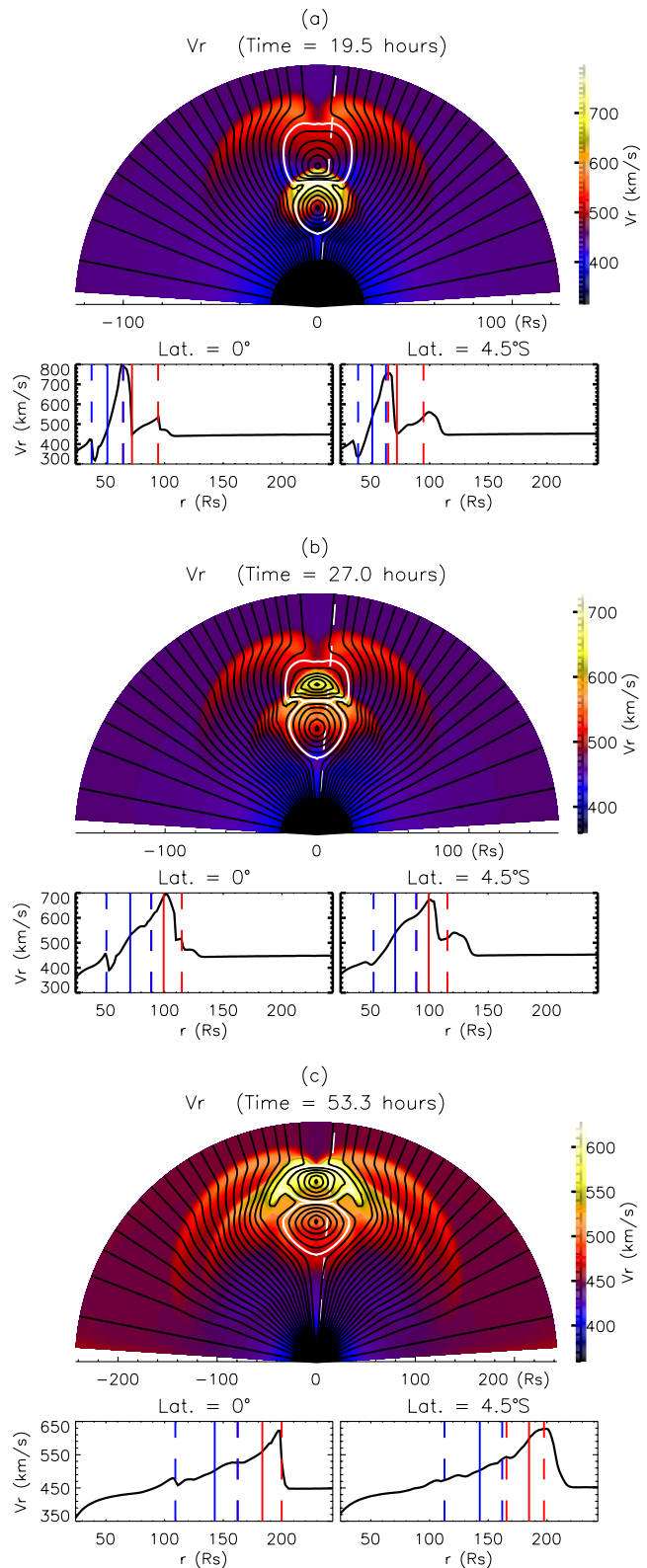
Figure 3. Evolution of MC2 overtaking MC1 for Case C_1 with radial flow speed v_r.
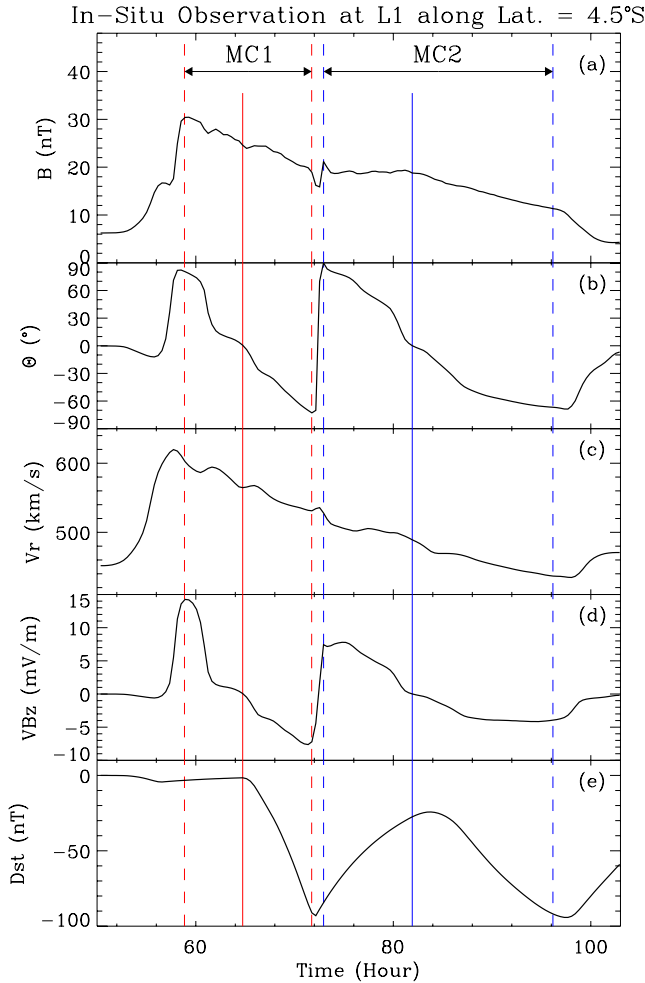
Figure 4. In situ hypothetical observation along Lat. = 4.5°S for Case C_1.

following MC2 to the slow preceding MC1. It results in monotonically decreasing v_r from the head to tail of Multi-MC at 53.3 h, as seen in Figure 3c. Besides, MC2 morphology turns from a radial-extent-elongated ellipse (Figure 3a) to an angular-extent-elongated one (Figure 3c) due to the blocking of MC1 body ahead. MC2 body is also compressed radially to some extent. Certainly, the compression of MC2 body is much less than that of MC1 body. Moreover, MC2-driven shock ultimately penetrates the MC1 body (Figure 3c) and will merge with the MC1-driven shock into a stronger compound shock, which is consistent with the previous results of double MC interaction [Odstrcil et al., 2003; Lugaz et al., 2005]. Therefore the Multi-MC has nearly been completing its final evolutionary stage at 53.3 h, after which the Multi-MC will move forward as a relatively stable structure.

[14] Time sequence of hypothetical measurement at L1 for Case C_1 is shown in Figure 4. The MC2-driven shock just emerges from MC1 body after penetrating it, so no extremum of speed profile v_r is found inside the multicloud. Double dips of Dst index are −93 nT and −95 nT, increased by 47 nT and decreased by 20 nT, respectively, in contrast with those in Case B_1 in Figure 2e. The mitigation of geoeffectiveness for the first Dst dip is owing to the position

of MC2-driven shock front far away from the rear part of MC1 with southward magnetic component, the aggravation for the second Dst dip is ascribed to the MC2 body compression mentioned above. A peak of VB_z up to 14 mV/m can be seen near the MC1 front boundary, where the largest compression occurs. However, it is positive and makes no contribution to geoeffectiveness. Additionally, the durations of MC1 and MC2 are shortened by 4.7 and 3 h, respectively, as compared with those in Case B_1.

[15] Figure 5 shows the time-dependent parameters of Multi-MC Case C_1 (thick curves), where the dotted, dashed, and dotted vertical lines from left to right denote the occasion of MC2-driven shock encountering MC1 body tail, MC2 body hitting MC1 body tail, and MC2-driven shock reaching MC1 body head, respectively. Two corresponding isolated MC cases are superimposed as thin curves for comparison. The acceleration of MC1 is large and early, while the deceleration of MC2 is small and late, as seen from Figure 5a. The radial compression of MC2 body brings not only the shortening of its radial span Sr but also the stretching of its angular span $S\theta$. The behavior of MC1 is a bit more complex. In our previous studies of MC-shock interaction [Xiong et al., 2006a, 2006b], MC compressed morphology will be restored after the shock passage. However, in the presence of the following MC2 body's pushing effect for Multi-MC case, MC2 body will take over the role of suppressing MC1's inherent magnetic elasticity when MC2-driven shock moves farther. Thus the firm gripping of MC1 body at all time leads to significant shrinking of its volume. It is why cross section area of MC1 body is smaller than that of MC2 (Figure 5d). Particularly, as seen from the local minimum value of Sr at 30 h in Figure 5b, the compression of MC1's Sr reaches to its extreme when the MC2-driven shock nearly arrives at MC1 head boundary. Meanwhile, the temporarily enhanced $S\theta$ of MC1 during 24 ∼ 38 h is steadily reduced afterward (Figure 5c).

3.3. MC2 Helicity Role

[16] There are various combination modes to form a double-MC structure on basis of each subcloud helicity signature [Wang et al., 2002], one of which possessing the strongest geoeffectiveness is positive helicity for preceding MC1 ($H_{mc1} = 1$) and negative helicity for following MC2 ($H_{mc2} = -1$) [Wang et al., 2004]. According to this scenario [Wang et al., 2004], simulation cases B_2 and C_2 are run simply by reversing MC2 helicity in Cases B_1 and C_1, respectively. The in situ record of passage of multicloud event at L1 is shown in Figure 6, with columns A and B corresponding to cases B_2 and C_2, respectively. In contrast to Figures 2 and 4, the elevation angle Θ of magnetic field vector within the double-flux-rope structure in Figure 6 is changed from the north-south-north-south orientation to north-south-south-north one. Though two Dst dips exist in groups EID_2 and CID_2, close scrutiny reveals that (1) the recovery phase of the first trivial Dst dip is extremely short (3.3 and 0.9 h in cases B_2 and C_2, respectively); (2) the second Dst dip is low enough to describe the whole geoeffectiveness by its local minimum, with −166 nT at 90 h in case B_2 and −144 nT at 78 h in case C_2. Hence from the perspective of continuous interval with southward magnetic field B_s, Dst curve in groups EID_2 and CID_2 can be
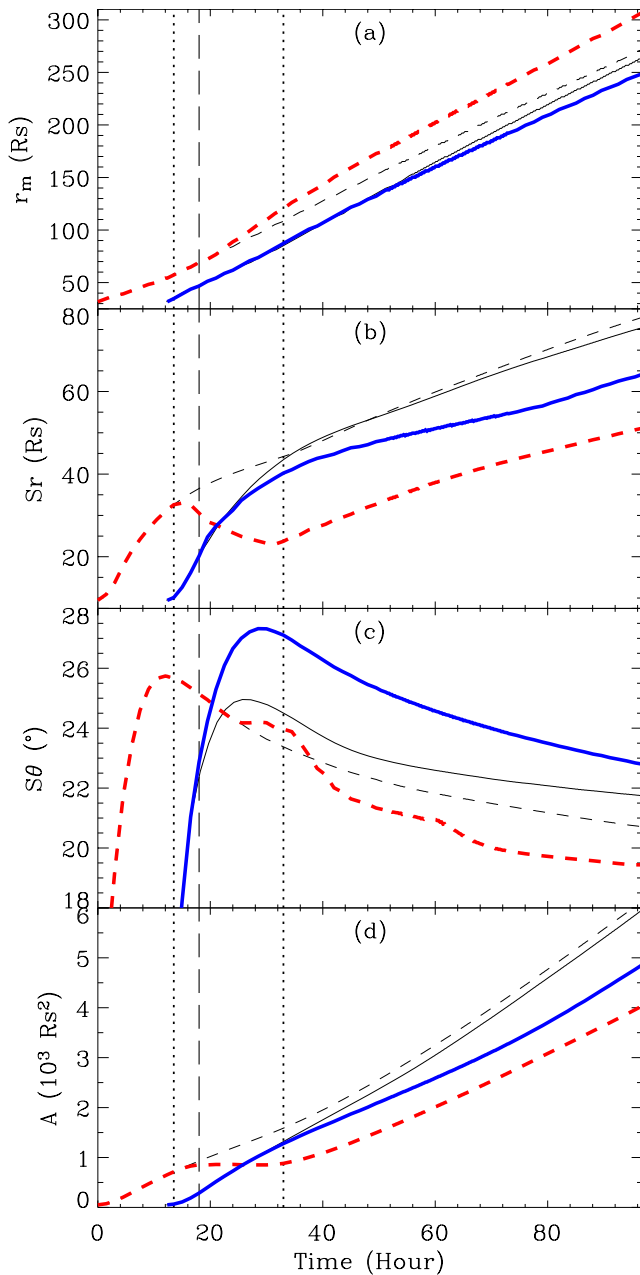
Figure 5. Time dependence of MC parameters: (a) radial distance of MC core r_m, (b) MC radial span Sr, (c) MC angular span $S\theta$, and (d) MC cross section area A. The thick dashed and solid lines denoted the preceding MC1 and following MC2 in Multi-MC Case C_1, superimposed with thin lines for corresponding individual MC cases for comparison. Three vertical delimiting lines (dotted, dashed, and dotted) from left to right correspond to the occasion of MC2-driven shock encountering MC1 body tail, MC2 body hitting MC1 body tail, and MC2-driven shock reaching MC1 body head, respectively.

considered as a one-dip structure by ignoring the first trivial dip. The closer the distance between two sources of IP geoeffective trigger, the easier is the superposition of individual geoeffectiveness, the greater is the resulting geomagnetic storm. This is confirmed by contrast of Figures 6c and 6f with Figures 2e and 4e.

4. Geoeffectiveness Studies

[17] Near-HCS latitudinal dependence of the Dst index is plotted in Figure 7, where Dst_{P1} (Figure 7a) and Dst_{P2} (Figure 7b) represent the first and the second Dst dips in cases B_1 and C_1, while Dst_N (Figure 7c) depicts the single Dst dip in cases B_2 and C_2. The dashed and dash-dotted lines represent for cases B_1 and C_1, respectively, in Figures 7a and 7b and they represent for Cases B_2 and C_2, respectively, in Figure 7c. As the MC2-driven shock continues to propagate through the MC1 medium, Dst_{P1} increases within Lat. $> 1.3°$ and decreases within Lat. $< 1.3°$, found in Figure 7a. Meanwhile the distribution of Dst_N in Figure 7c is quite similar. The trend of decreased Dst near HCS is opposite to that in the case of MC-shock interaction [cf. *Xiong et al.*, 2006a, Figure 8]. The above divergence is clarified by the absence of following MC body pushing in MC-shock interaction [*Xiong et al.*, 2006a]. First, the latitudinal extent of MC2 body is much narrower than that of MC2-driven shock. Second, the coalescent boundary between MC1 and MC2 body is further narrower, which covers latitude range between 4.5°S and 4.5°N (Figure 3c). Thus the MC2 body pushing effect is strongest at the equator, within confined latitudinal extent between 4.5°S and 4.5°N. The near-HCS geoeffectiveness of Dst_{P1} from Case B_1 to Case C_1, Dst_N from Case B_2 to Case C_2 is subsequently aggravated. As a result, nonuniform latitudinal distribution of Dst_{P1} and Dst_N is intensified. Besides, Dst_{P2} is nearly unaffected in Case B_1. However, Dst_{P2} in Case C_1 is obviously decreased, as a result from the compression of MC2 body interpreted in section 3.2. Hence the geoeffectiveness of Multi-MC is indeed largely enhanced due to interaction between subclouds, as compared with that in an isolated MC event.

[18] In order to quantify the evolution process of multi-cloud, $d_0 = r_{mc2} - r_{mc1}$, the distance between the cores of MC2 and MC1 on the occasion of MC1 head just reaching L1, is chosen as an indicative parameter. Here r_{mc1} and r_{mc2} are the core positions of MC1 and MC2 in radial direction, respectively. The reliance of several multicloud parameters on d_0 is further explored in Figure 8 by the integrated study of Groups EID_1 and EID_2. The absolute value of d_0 is labeled as $|d_0|$. As Dt, the emergence interval of MC1 and MC2, decreases, $|d_0|$ firstly reduces from 107 to 53 R_s at a constant slope, then asymptotically approaches to 42 R_s shortly after MC2-driven shock emerges from MC1 body head (Figure 8a). The penetration depth of MC2-driven shock in MC1 medium, d_{Dst}, defined by the radial distance between MC2-driven shock front and MC1 inner boundary along the equator, is shown in Figure 8b, which can be divided into four stages according to the different behaviors: (1) a rapid increase during $d_0 < -66.3 \ R_s$, (2) an extremely slow increase during $-66.3 \ R_s < d_0 < -52.5 \ R_s$, (3) a fast reincrease during $-52.5 \ R_s < d_0 < -46.7 \ R_s$, (4) a very small oscillation around the final limit value of 40 R_s during $d_0 > -46.7 \ R_s$. The rapid increasing of d_{Dst} in stages 1 and 3 is straightforward due to continuous forward movement of shock front in MC1 medium. As for stage 2, during which
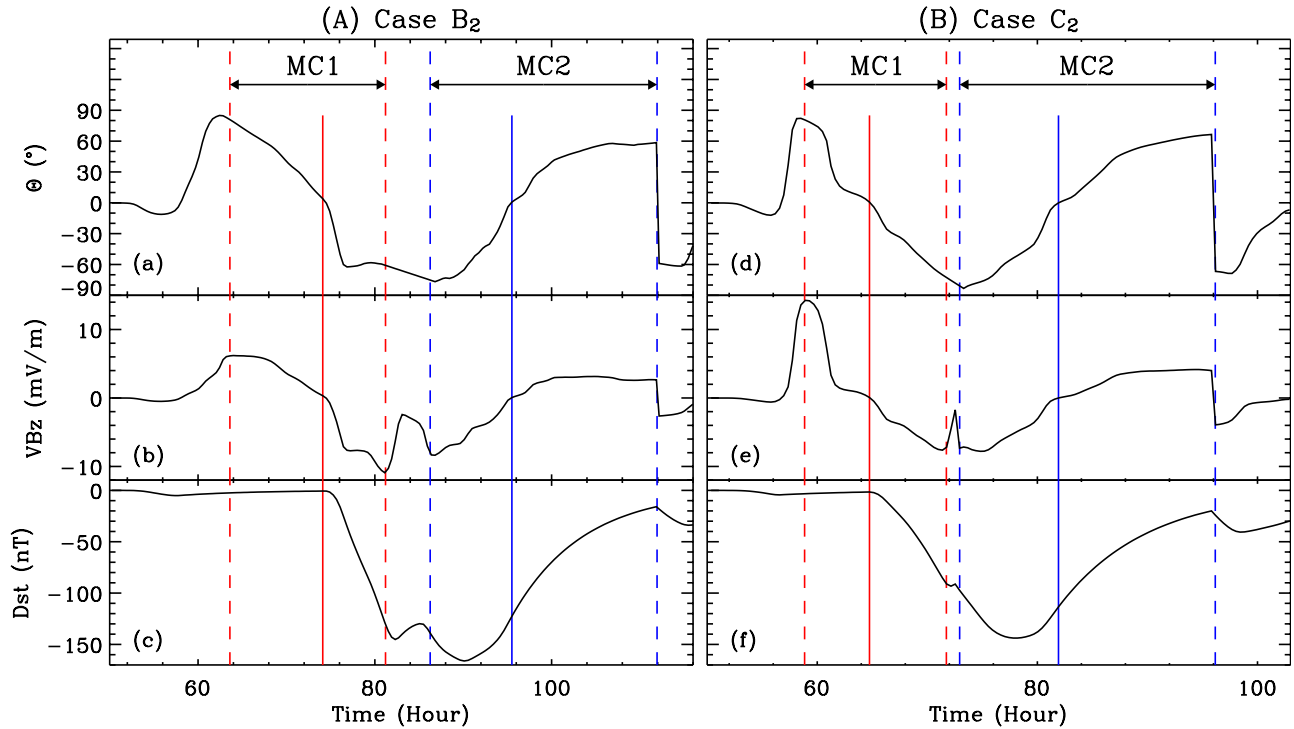
Figure 6. In situ hypothetical observation along Lat. = 4.5°S for (a) Case B_2 and (b) Case C_2. Cases B_2 and C_2 differ from their respective companion Cases B_1 and C_1 by the opposite MC2 magnetic helicities.

the shock front hits MC1 core, though the shock front location relative to the MC1 body is deeper and deeper at that time, the abrupt change of MC1 rear boundary morphology from a V-shape to a straight line, mentioned in section 3.2, greatly reduces the radial extent of MC1 rear half, and hence significantly inhibits the increase of the absolute value of penetration depth d_{Dst}. When the shock front crosses the MC1 front boundary ($d_0 > -46.7\ R_s$), the magnetic tension of the highly compressed MC1 body is

drastically accumulated. As a result, the nearer the distance between two sub-MCs is (the shorter the $|d_0|$ is), the larger is the resistance of MC1 elasticity against compression. The final equilibrium is naturally manifested in the behavior of stage 4. The early and sensitive response of Max.(B_{mc1}) at $d_0 = -100 R_s$ is conspicuous along Lat. = 4.5° in Figure 8c because the initial interaction between MC1 body and MC2-driven shock happens around Lat. = 4.5°. The swift enhancement of Max.(B_{mc1}) during $-68.9\ R_s < d_0 < -46.7\ R_s$
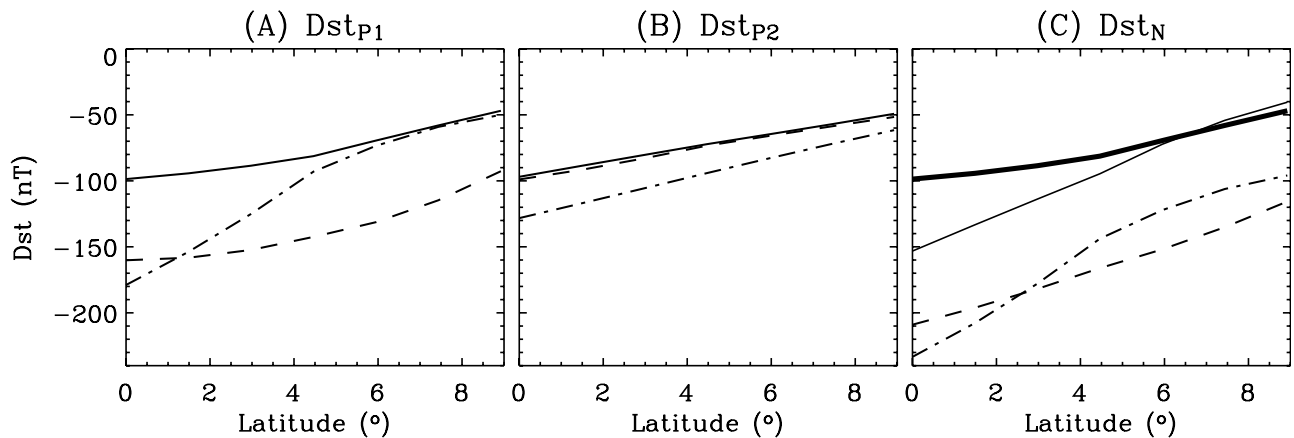
Figure 7. Comparison of latitudinal distribution of *Dst* index among the Multi-MC Cases B_1, C_1, B_2, and C_2. Double *Dst* dips in Cases B_1 and C_1 with positive magnetic helicities in MC2 are shown in (a) Dst_{P1} and (b) Dst_{P2}, as well as a single *Dst* dip in Cases B_2 and C_2 with negative helicity in MC2 shown in (c) Dst_N. Dashed and dash-dotted lines in Figures 7a and 7b correspond to Cases B_1 and C_1 respectively; dashed and dash-dotted lines in Figure 7c correspond to Cases B_2 and C_2 respectively. The isolated events corresponding to MC1 and MC2 for Case B_1 are denoted as solid lines in Figures 7a and 7b, those for Case B_2 as solid thick and thin lines in Figure 7c.
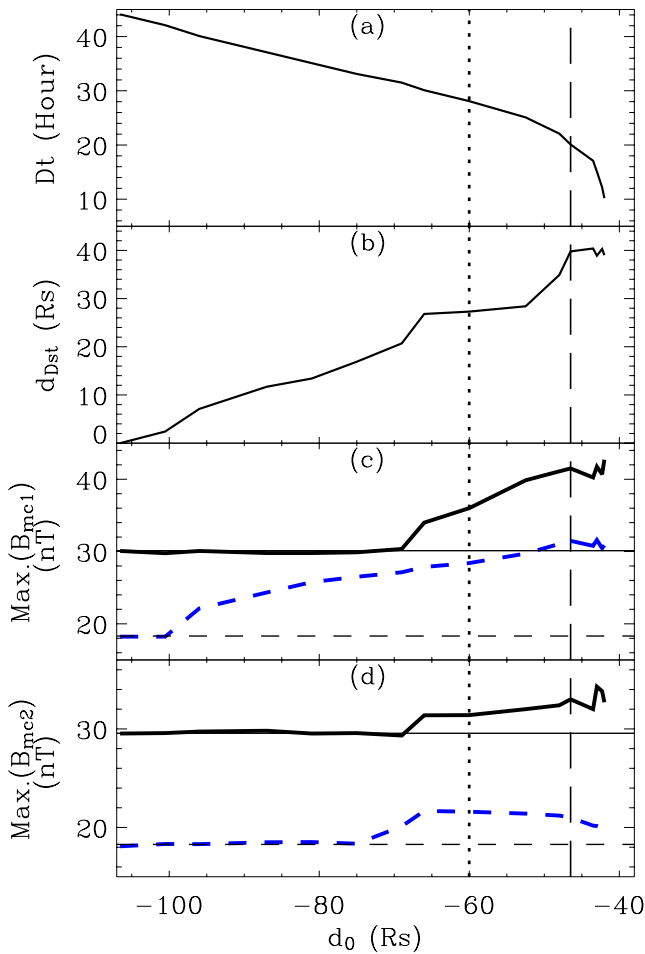
Figure 8. The d_0-dependent parameter variances at L1 in Group EID_1: (a) Dt, time interval of MCs ($Dt = t_{mc2}-t_{mc1}$, $t_{mc1} = 0$ h); (b) d_{Dst}, penetration depth of MC2-driven shock in MC1 medium; (c) Max.(B_{mc1}), the maximum of magnetic field strength in MC1; and (d) Max.(B_{mc2}), the maximum of magnetic field strength in MC2. Here d_0 refers to the distance between MC2 core r_{mc2} and MC1 core r_{mc1} on the occasion of MC1 head just reaching L1, namely $d_0 = r_{mc2} - r_{mc1}$. The vertical delimiting dotted and dashed lines denote the occasions of MC2-driven shock just hitting MC1 core and head at L1. In Figures 8c and 8d the thick solid and dashed lines denote observations along Lat. = 0° and 4.5°S, while the thin horizontal ones represent the values of corresponding isolated MC events.

along Lat. = 0° is owing to the compression concurrently exerted by the MC2-driven shock and MC2 body. Both Max.(B_{mc1}) and Max.(B_{mc2}) reach a relatively stable state when $|d_0| = 42R_s$.

[19] The variance of geoeffectiveness as a function of d_0 is elucidated in Figure 9. The analyses on Dst_{P1}, Dst_{P2}, and Dst_N are addressed one by one. First, when $d_0 < -60$ R_s, the behavior of all parameters in Figures 9a–9d for Dst_{P1} is pretty coincident with that of our previous study for MC-shock interaction [cf. *Xiong et al.*, 2006a, Figures 9b–9e]. The dynamics of MC1-MC2 merging at that time is dominated by the interaction between MC2-driven shock and MC1 body. Thus MC2-driven shock plays the similar role

of the incidental shock as addressed before [*Xiong et al.*, 2006a], which clarifies the above-mentioned coincidence. As $|d_0|$ is reduced from $60R_s$ to 52.5 R_s, MC2 body directly collides with MC1 body. It leads to the decrease of Dst, Min.(VB_z), and Min.(B_s) due to compression. Particularly, the decrease of Min.(VB_z) and Min.(B_s) along Lat. = 4.5°S is very drastic because the change of MC1 field line morphology from a V-shape to a straight line mentioned in section 3.2 leads to the southward rotation of magnetic field within MC1 rear half along Lat. = 4.5°S. This additional rotation effect further strengthens B_s along Lat. = 4.5°S. When $|d_0|$ continues to decrease to be less than 52.5 R_s, significant difference of geoeffectiveness between Lat. = 0° and 4.5°S occurs. Along Lat. = 4.5°S, the rapid recovery of Min.(B_s) from −24.5 to −13.5 nT, and Min.(VB_z) from −15 to −8 mV/m, leads to the subdued Dst_{P1} from its minimum −165 to −100 nT. Contrarily, the geoeffectiveness along Lat. = 0° remain unchanged (Figures 9a–9d). Namely, the aggravated geoeffectiveness along the equator is the same with $Dst_{P1} = −180$ nT, provided that $|d_0|$ is smaller than a certain threshold of 52.5 R_s. This highly nonuniform latitudinal distribution of Dst_{P1} is owing to the limited latitudinal range (4.5°S ∼ 4.5°N) of pushing effect of MC2 body. When the shock ultimately penetrates MC1 body, the persistent pushing of following MC2 body within 4.5°S ∼ 4.5°N can prevent the previously compressed magnetic field lines of MC1 body from being relaxed. So Dst_{P1} along Lat. = 0° is nearly constant for $|d_0| < 52.5$ R_s. As for Dst_{P1} along Lat. = 4.5°S, it increases as a result of relaxation of magnetic tension without MC2 body pushing. Second, the variance of Dst_{P2} (geoeffectiveness of sub-MC2) only happens between $d_0 = −68$ R_s and −46.7 R_s, during which the MC2 body compression due to the blocking of MC1 body takes effect. Before the involving of MC2 body into interaction ($d_0 < −68$ R_s), or after the completion of Multi-MC's drastic evolution stage ($d_0 > −46.7$ R_s), Dst_{P2} is unchanged. By comparing Dst_{P2} with Dst_{P1}, one can see that the MC1 undergoes the greater compression than the MC2. Third, the behavior of Dst_N (Figures 9i–9l) is quite similar to that of Dst_{P1} (Figures 9a–9d) due to similar reasons mentioned above. The minimum Dst in Figures 9a, 9e and 9i is −180, −130, and −235 nT, respectively. The greatest geoeffectiveness of Dst_N directly results from the longest Δt (Figure 9k). Therefore the geoeffective parameters of every sub-MC are dramatically changed in contrast with those of the corresponding isolated MC during the merging process. For the IP compound structure formed by multiple ICMEs, the geoeffectiveness is jointly determined by two factors: the parameters of the individual ICMEs themselves, and the interaction process between these ICMEs. This is substantiated by the observation data analyses [*Wang et al.*, 2002, 2003a; *Xue et al.*, 2005; *Farrugia et al.*, 2006; *Zhang et al.*, 2007] and our quantitative investigation of numerical simulation of this study.

[20] The multicloud geoeffectiveness depends on not only the MC1-MC2 eruption interval but also collision intensity. Obviously, an MC1 overtaken by an MC2 with various initial speeds may result in different geoeffectiveness. From the Figure 9 concerning Groups EID_1 and EID_2, two basic results are obtained: (1) The maximum geoeffectiveness occurs at Lat. = 0° for the same propagation direction of MC1 and MC2 along the equator; (2) the final Dst at Lat. = 0°
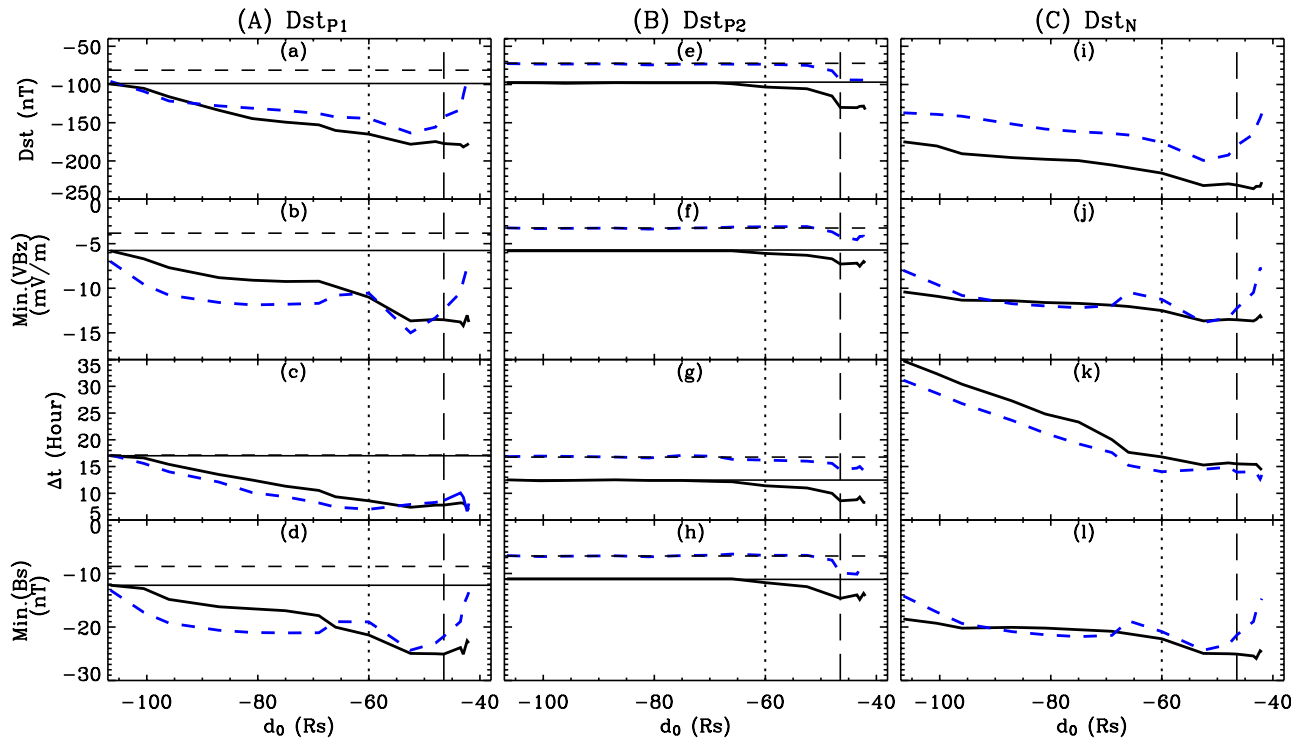
Figure 9. Parameter variances of Multi-MC geoeffectiveness as a function of d_0: (a, e, i) Dst index; (b, f, j) Min.(VB_z), the minimum of dawn-dusk electric field VB_z; (c, g, k) Δt, the interval between the commencement of $VB_z < -0.5$ mV/m and the corresponding minimum Dst; and (d, h, l) Min.(Bs), the minimum of southward magnetic component. Solid and dashed lines correspond to observations along Lat. = 0° and 4.5°S, respectively. The double Dst dips in Group EID_1 are shown by columns A (Dst_{P1}) and B (Dst_{P2}), and the single Dst dip in Group EID_2 is shown by column C (Dst_N). The horizontal solid, and dashed lines denote observations of the isolated events, corresponding to Group EID_1, at Lat. = 0° and 4.5°S, respectively, with MC1 in column A and MC2 in column B.

is nearly constant, provided the accompanying $|d_0|$ is sufficiently small ($|d_0| \leq 46.7\ R_s$) or the initial MC1-MC2 eruption interval is sufficiently short ($Dt \leq 20$ h). With t_{mc2} designated to be 12.2 h, the reliance of geoeffectiveness along the equator on collision degree is further explored in Figure 10 by parametric study of variable v_{mc2}. The larger the value of v_{mc2} is, the greater is the collision degree that the Multi-MC may suffer from. Dst_{P1} only decreases a bit from -180 to -210 nT within such a wide spectrum of v_{mc2} from 450 to 1200 km/s. The geoeffectiveness enhancement of Multi-MC is ascribed to compression between the sub-MCs. When the MC1 compression has already approached to saturation, the effect to increase MC1 geoeffectiveness by having MC1 impinged by a highly fast MC2 is extremely limited. It is more and more difficult to quench the dramatically accumulated magnetic elasticity of MC1 body, as MC1 undergoes the greater and greater compression. The impact of the high-speed MC2 body is largely offset by the buffer action of magnetic tension of the MC1 body. As for Dst_{P2}, the increase of v_{mc2} has a direct influence. However, Dst_{P2} deducted by the Dst of the corresponding individual MC2 event is roughly constant, which can be seen from Figure 10b. Namely, Dst_{P2} decreases from -125 to -190 nT, as v_{mc2} increases from 450 to 1200 km/s, chiefly ascribed to the increase of geoeffectiveness of the corresponding individual MC2 event itself, but not MC1-MC2 interaction. Excluding the geoeffectiveness increase of

individual MC2 event, Dst_N still decreases for $v_{mc2} > 1000$ km/s in Figure 10c because interaction takes obvious effect herein. The geoeffectiveness variance can be elucidated from the perspective of dynamic response of sub-MCs. The double-MC interacting region is within MC1 rear part and MC2 front part, where the direct compression occurs. So the factor of MC1-MC2 interaction for geomagnetic storm enhancement is strongest for Dst_N, weakest for Dst_{P2}. In conclusion, two points can be drawn from Figures 9 and 10: (1) The significant geoeffectiveness variance accompanies the different evolution stages; (2) once a Multi-MC completes its evolution process before its arrival at 1 AU, the collision intensity between sub-MCs merely modulates the final geoeffectiveness a bit. The innate magnetic elasticity can buffer the reciprocal collision between sub-MCs against each other. When every sub-MC becomes stiffer and stiffer, the compression reaches its asymptotic degree, and the geoeffectiveness enhancement becomes less and less obvious. Therefore with respect to Multi-MC geoeffectiveness, the evolution stage is a dominant factor, whereas the collision intensity is a subordinate one.

[21] Additionally, the dependence of geoeffectiveness of an individual MC on the eruption speed v_{mc} is also revealed from the isolated MC2 events from Figure 10. If B_s region in MC medium is located in its anterior half (Group IM_2), Dst steadily decreases as v_{mc} increases, as seen by the thin
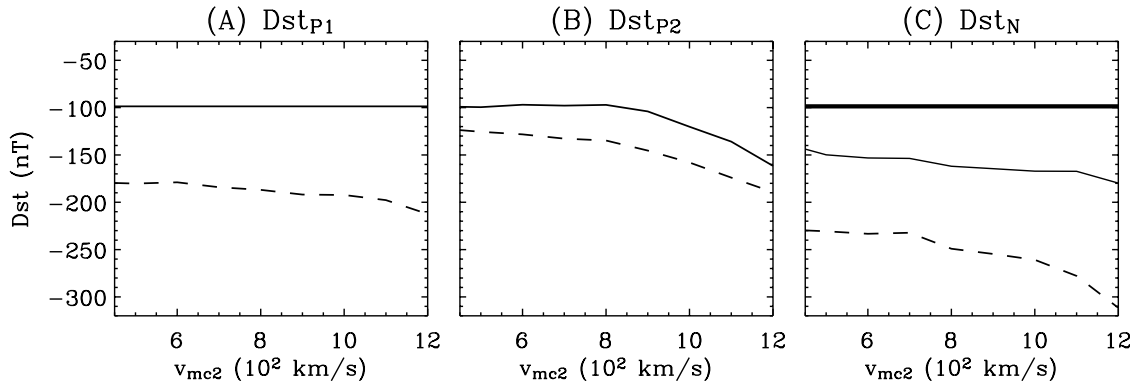
Figure 10. Reliance of *Dst* in Multi-MC cases on initial speed of following MC2. Double *Dst* dips in Group CID_1 are shown as dashed lines by (a) Dst_{P1} and (b) Dst_{P2}, while a single *Dst* dip in Group CID_2 by (c) Dst_N. Decoupled MC1 and MC2 events in Group CID_1 are plotted as solid lines in Figures 10a and 10b, those in Group CID_2 are shown as thick and thin solid lines in Figure 10c. The curves of single MC2 event in Figures 10b and 10c are nonhorizontal due to v_{mc2} variance.

solid line in Figure 10c; contrarily, if B_s region is to be in the rear half of MC (Group IM_1), *Dst* only decreases on the condition of $v_{mc} > 800$ km/s, as seen by the solid line in Figure 10b. The increase of v_{mc} leads to a more violent interaction of individual MC body with the ambient solar wind ahead. As a result, MC core, initially located at the geometry center of MC boundary, will be gradually shifted to MC anterior boundary. MC anterior half is preferential compressed because MC-ambient flow interaction originates from MC front boundary. The compression exists in MC rear half, only when the whole cross section area of MC body is significantly contracted on the condition of very fast speed v_{mc}. This is why *Dst* for Group IM_1 remains a constant of -100 nT within $v_{mc} = 450 \sim 800$ km/s.

5. Compressibility Analyses

[22] The idea that the compression is an efficient mechanism to enhance the geoeffectiveness of the preexisting B_s event has been proved in data analyses [*Wang et al.*, 2003c]. Compression effect is virtually responsible for the geoeffective property of Multi-MC. So it is very meaningful to analyze the maximum compression degree for a Multi-MC.

[23] The Multi-MC characteristics can be inferred from several parameters of near-Earth measurements, depicted by Figure 11. The interchange of momentum between the preceding slow cloud MC1 and following fast cloud MC2 leads to MC1 acceleration and MC2 deceleration, which influences, more or less, the Sun-Earth transient time, TT_{mc1} and TT_{mc2} for MC1 and MC2, respectively. The shortening of TT_{mc1} begins at $Dt = 21$ h as seen from Figure 11a, meanwhile the lengthening of TT_{mc2} begins at $Dt = 28$ h, seen from Figure 11b. The MC1 acceleration is very obvious, as the larger v_{mc2} is, the smaller is TT_{mc1} (Figure 11g). Contrarily, the MC2 slowdown is independent of v_{mc2}, as TT_{mc2} in coupled events deviates from that in the corresponding isolated events by a constant (Figure 11h). The effect of TT_{mc1} decrease is much greater than that of TT_{mc2} increase for Multi-MC cases. Since the transporting time of an ICME may be modified if it interacts with others during its IP propagation, some empirical formulas of

transporting time on basis of observations of one single ejecta event [*Gopalswamy et al.*, 2000, 2001a] cannot be directly applied to the ICME-ICME interaction cases [*Farrugia and Berdichevsky*, 2004; *Y. M. Wang et al.*, 2005; *Xiong et al.*, 2005]. Coupling between ICMEs occupies a large fraction for the causes of great geomagnetic storms [*Xue et al.*, 2005; *Zhang et al.*, 2007], the Multi-MC should be paid special attention for space weather predicting. Thus the numerical simulation based on physics models is very useful to forecast the arrival time of the interacting ICMEs. The duration of sub-MC passage at L1, ΔT_{mc}, is a distinct reflection of compression effect. ΔT_{mc1} exists a lower limit, as shown in Figure 11c, so does ΔT_{mc2} in Figure 11d. When the Multi-MC experiences the sufficient evolution for $Dt < 24$ h, the reduction of ΔT_{mc1} and ΔT_{mc2} is 14 and 4.5 h, respectively, in contrast with the corresponding isolated sub-MC cases. As v_{mc2} increases, both ΔT_{mc1} and ΔT_{mc2} monotonically decrease. However, the solid and dashed lines, representing the Multi-MC and corresponding isolated MC events in Figure 11j, intersect at $v_{mc2} = 1040$ km/s. ΔT_{mc2} in MC1-MC2 interaction is determined by two factors: (1) the compression of MC2 radial extent resulting from collision; (2) the slowdown of MC2 body as a result of momentum transfer from MC2 to MC1 body. The first factor, tending to shorten ΔT_{mc2}, dominates the cases for $v_{mc2} < 1040$ km/s; the second factor, trending to lengthen ΔT_{mc2}, dominates the cases for $v_{mc2} > 1040$ km/s. Besides, the near-Earth radial span of MC1 body Sr_{mc1} in Figures 11e and 11k has the similar variance trend as ΔT_{mc1} in Figures 11c and 11i. It again proves that the compression has saturation effect for MC1 body. The Sr_{mc1} of 67 R_s in an individual case can be compressed to 40 R_s at most by Dt reduction (Figure 11e). Sr_{mc1} decreases very slowly from 43 R_s at $v_{mc2} = 450$ km/s to 25 R_s at $v_{mc2} = 1200$ km/s (Figure 11k). Moreover, the overall compression degree for a Multi-MC is well described by d_0, the distance between the core of the following MC2 and preceding MC1 on the occasion of MC1 head just reaching L1. One can see that d_0 variance is associated with Multi-MC evolution stages (Figure 11f). The swiftly reducing trend of $|d_0|$ at the beginning is suddenly stopped at $Dt = 25$ h. Here $|d_0|$ reaches its lower limit of 42 R_s at $Dt = 17$ h and
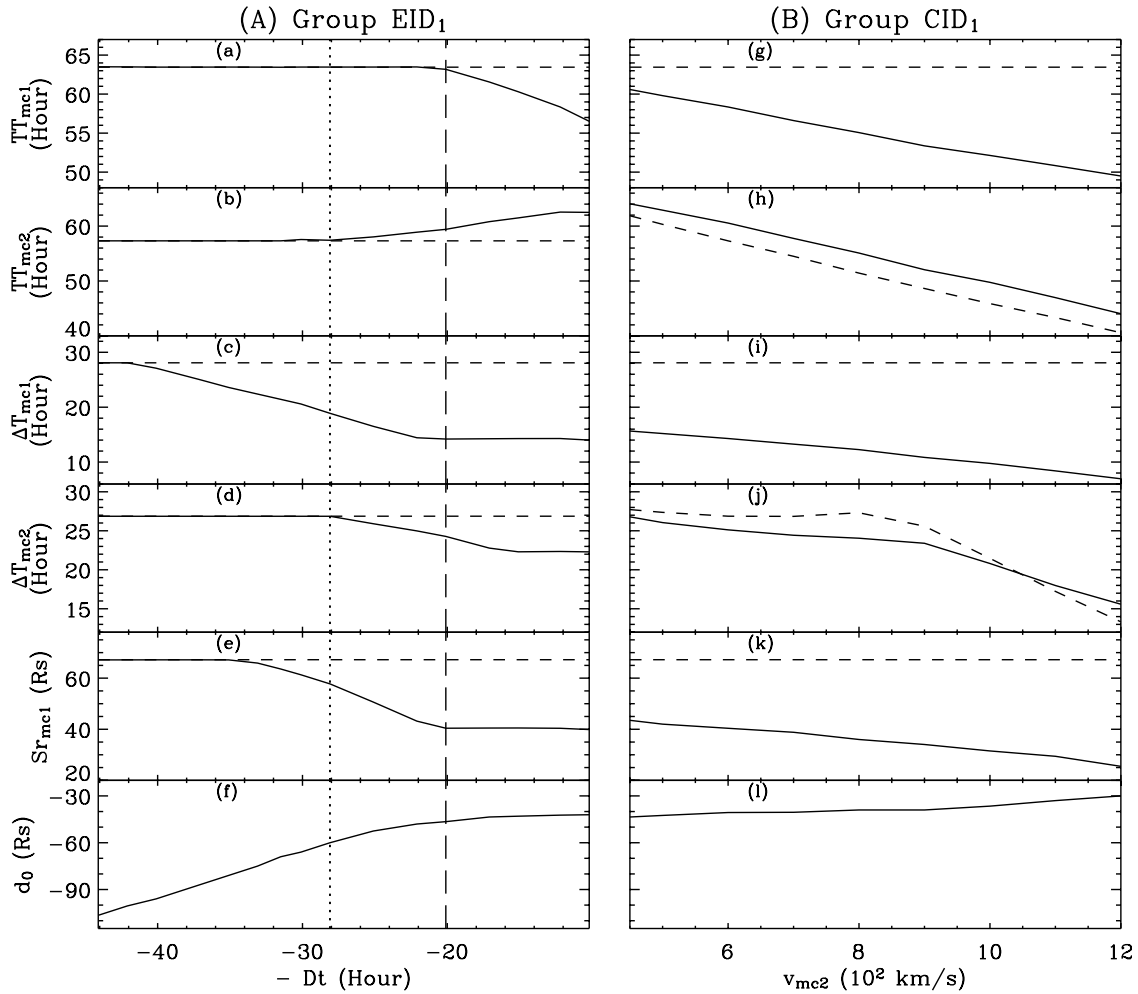
Figure 11. Dependence of Multi-MC characteristic parameters at L1 on MC2-MC1 eruption interval $-Dt$ ($-Dt = -1 \cdot Dt = t_{mc1} - t_{mc2}$) and MC2 speed v_{mc2} is shown by columns A (Group EID$_1$) and B (Group CID$_1$). Shown are (a, g) TT_{mc1}, the Sun-Earth transient time of MC1; (c, i) ΔT_{mc1}, MC1 event duration at L1; (e, k) Sr_{mc1}, MC1 radial span; and (f, l) d_0, the distance between MC2 and MC1 core. Figures 11a, 11c, 11g, 11i, and Figures 11b, 11d, 11h, 11j are the counterparts for MC1 and MC2, respectively. Figures 11e, 11f, 11k, and 11l refer to the occasion when MC1 head just reaches L1. Dashed lines in all figures except Figures 11f and 11l represent the corresponding isolated MC events for comparison. The vertical dotted and dashed lines in column A denote the cases of MC2-driven shock just hitting MC1 core and head, respectively.

maintains a horizontal slope afterward. When the inherent magnetic tension rivals the external compression for force balance, each sub-MC behaves like a rigid body with a little elasticity. Here $|d_0|$ is only reduced from 43 to 30 R_s over such a wide v_{mc2} range from 450 to 1200 km/s (Figure 11l).

[24] The compression due to interaction is primarily responsible for geoeffectiveness enhancement, once two MCs form a Multi-MC. Assuming nonexistence of magnetic field in the IP medium and all ejecta, the preceding ejecta may be exorbitantly compressed to an unbelievably small scale by the following ejecta [*Gonzalez-Esparza et al.*, 2004; *Gonzalez-Esparza*, 2005]. Obviously the compressibility on basis of hydrodynamic nature [*Gonzalez-Esparza et al.*, 2004; *Gonzalez-Esparza*, 2005] is overestimated due to ignoring of magnetic elasticity. The larger the compression is, the stiffer is every sub-MC body. Hence a cutoff compression degree exists because of magnetic tension.

Besides, if the helicity of MC1 is consistent with that of MC2, a electric current sheet occurs between the adjoining boundary of MC1 and MC2 due to magnetic field direction reversal. The electric current intensity synchronously increases with the Multi-MC compression. If magnetic reconnection happens there, the MC1-MC2 collision effect would be weakened. As a result, the outermost part of magnetic field lines of each sub-MC would be reconnected together [*Y. M. Wang et al.*, 2005]. Particularly in the condition of large speed difference between MC1 and MC2, both MCs may be merged into one new magnetic flux rope by the driven magnetic reconnection [*Odstrcil et al.*, 2003; *Schmidt and Cargill*, 2004; *A. H. Wang et al.*, 2005]. The magnetic reconnection reduces Multi-MC's cutoff compression degree. If magnetic reconnection is introduced into Groups EID$_1$ and CID$_1$ of Table 2, the Multi-MC geoeffectiveness would become weakening due

Table 2. Assortment of Simulation Cases of Multi-MC[a]

Group	Case	v_{mc2}, 10^2 km/s	t_{mc2}, h	Comment
EID_1	$B_1, C_1, D_1, E_1,$ $F_1, G_1, H_1, I_1,$ $J_1, K_1, L_1, M_1,$ N_1, O_1, P_1, Q_1	6	30.1, 12.2, 44.1, 42.1, 40.1, 37.1, 35.1, 33.1, 31.5, 28.1, 25.1, 22.1, 20.1, 17.1, 15.1, 10.2,	eruption interval dependence ($H_{mc1} = 1, H_{mc2} = 1$)
EID_2	$B_2, C_2, D_2, E_2,$ $F_2, G_2, H_2, I_2,$ $J_2, K_2, L_2, M_2,$ N_2, O_2, P_2, Q_2	6	30.1, 12.2, 44.1, 42.1, 40.1, 37.1, 35.1, 33.1, 31.5, 28.1, 25.1, 22.1, 20.1, 17.1, 15.1, 10.2,	eruption interval dependence ($H_{mc1} = 1, H_{mc2} = -1$)
CID_1	$R_1, S_1, C_1, T_1,$ $U_1, V_1, W_1, X_1,$ Y_1	4.5, 5, 6, 7, 8, 9, 10, 11, 12	12.2	collision intensity dependence ($H_{mc1} = 1, H_{mc2} = 1$)
CID_2	$R_2, S_2, C_2, T_2,$ $U_2, V_2, W_2, X_2,$ Y_2	4.5, 5, 6, 7, 8, 9, 10, 11, 12	12.2	collision intensity dependence ($H_{mc1} = 1, H_{mc2} = -1$)

[a]Note that $v_{mc1} = 400$ km/s, $t_{mc1} = 0$ h for all 48 cases.

to the subdued compression and south magnetic component annihilation. However, magnetic diffusion in the IP space should be very small, magnetic reconnection may sightly modulate, but not significantly distort the dynamics and geoeffectiveness of Multi-MC in the framework of ideal MHD process. So the CME-CME cannibalization, firstly observed in the inner corona by the SOHO/Lasco [*Gopalswamy et al.*, 2001b], later proved to be caused by magnetic reconnection [*A. H. Wang et al.*, 2005], may not occur in the IP space [*Y. M. Wang et al.*, 2005].

6. Conclusions and Summary

[25] In order to better understand the nature of IP Multi-MC structure, the interaction between two IP MCs (MC1 and MC2), and the ensuing geoeffectiveness are explored under a very simplified and specialized circumstance by a 2.5-dimensional ideal MHD numerical model. This work is a continuation to our recent studies of MC-shock interaction [*Xiong et al.*, 2006a, 2006b] by replacing a following incidental strong shock with a following fast MC. Via analyses of a comprehensive integration of many simulation cases under various conditions, it is found that the magnetic elasticity, magnetic helicity of each MC, and compression between each other are the overriding physical factors in the formation, propagation, evolution, and resulting geoeffectiveness of IP Multi-MC.

[26] First, the dynamical response of MCs colliding is studied. The coupling of two MCs could be considered as the comprehensive interaction between two systems, each comprising of an MC body and its driven shock. Because the following MC2 is faster than the preceding MC1, the MC2-driven shock and MC2 body successively impact the rear boundary of MC1 body. As a result, the morphology of magnetic field lines at MC1's rear part is consequently changed from its initial rough semicircle to a V-shape and then to a flat line. As swept by the marching MC2-driven shock front, the local magnetic field lines in MC1 medium just downstream of MC2-driven shock front would be compressed and rotated. The pushing of MC2 body prevents the previously compressed magnetic field in MC1 medium from being restored, after the passage of MC2-driven shock front. MC1 body undergoes the most violent

compression from the ambient solar wind ahead, continuous penetration of MC2-driven shock through MC1 body, and persistent pushing of MC2 body at MC1 tail boundary, which leads to a significant shrinking of MC1's cross section. Contrarily, the blocking of MC1 body also results in the change of MC2 boundary from a radial-extent-elongated ellipse to an angular-extent-elongated one. The Momentum is continuously transferred from sub-MC2 to sub-MC1, until the radial profile of Multi-MC speed is monotonically decreasing with the maximum value at MC1-driven sheath. When MC2-driven shock is merged with MC1-driven shock into a stronger compound shock, Multi-MC completes its ultimate evolutionary stage, and hence moves forward as a relatively stable entity.

[27] Second, the geoeffectiveness of MCs coupling is explored. The interaction of MC1 and MC2 in the IP space results in the superposing of their geoeffectiveness. The two-MC event is associated with a two-step geomagnetic storm, as indicated by two *Dst* dips. Particularly, if B_s region in a Multi-MC is located at MC1 rear half and MC2 anterior half, the Multi-MC excites the greatest geomagnetic storm among all combinations of each sub-MC helicity, and two *Dst* dips can be nearly reduced to a single *Dst* dip due to ignoring of the very short recovery phase of the first *Dst* dip. The geoeffectiveness of each individual MC is largely enhanced as a result of MC1-MC2 interaction. Moreover, because latitudinal extent of MC body is much narrower than that of its driven shock, the effect of MC2 body pushing upon MC1 body is limited within a very narrow latitudinal band centered at the heliospheric equator. Outside this latitudinal band, geoeffectiveness is initially enhanced and then recovered, as the emergence interval of two MCs becomes shorter and shorter; meanwhile the geoeffectiveness is firstly aggravated and then maintains constant inside this band. Obviously, the nonuniform latitudinal distribution of geoeffectiveness is further intensified by MC2 body pushing. Moreover, With respect to Multi-MC geoeffectiveness, the evolution stage is a dominant factor, whereas the collision intensity is a subordinate one.

[28] Third, Multi-MC's compressibility associated with magnetic elasticity is analyzed. Both compression degree and evolutionary stage of a Multi-MC could be quantitatively described by $|d_0|$, the absolute distance between MC1

and MC2 core on the occasion of MC1 head just reaching L1. The shorter the $|d_0|$ is, the greater is Multi-MC's compressibility. Magnetic field lines of MC1 body initially appears to be too frail to resist the collision in the face of the overtaking high-speed MC2, so $|d_0|$ is steadily reduced. As the evolution of Multi-MC proceeds, the MC1 body suffers from larger and larger compression, and its original vulnerable magnetic elasticity becomes stiffer and stiffer. When the accumulated inherent magnetic elasticity in the highly shrunk MC1 body can counteract the external compression, the previous continuously reducing $|d_0|$ drastically approximates to an asymptotic limit. Magnetic elasticity not only buffers the collision between MCs, but also leads to a cutoff compression degree of Multi-MC. Moreover, the collision of MC2 with a very wide speed spectrum upon MC1 has a little influence to enhance the cutoff compressibility. However, if magnetic reconnection occurs within the interacting region of Multi-MC, the cutoff compressibility would be expected to decrease a bit.

[29] Overall, the Multi-MC is of great concern for space weather community. The geoeffectiveness enhancement of coupling of multiple MCs is virtually ascribed to compression in the Multi-MC. The maximum compressibility of Multi-MC is mainly decided by its inherent magnetic elasticity.

References

Baker, D. N. (2002), How to cope with space weather, *Science*, 297, 1486–1487.

Berdichevsky, D. B., I. G. Richardson, R. P. Lepping, and S. F. Martin (2005), On the origin and configuration of the 20 March 2003 interplanetary shock and magnetic cloud at 1 AU, *J. Geophys. Res.*, 110, A09105, doi:10.1029/2004JA010662.

Burlaga, L. F. (1988), Magnetic clouds and force-free fields with constant alpha, *J. Geophys. Res.*, 93, 7217–7224.

Burlaga, L. F., E. Sittler, F. Mariani, and R. Schwenn (1981), Magnetic loop behind an interplanetary shock: Voyager, Helios, and IMP 8 observations, *J. Geophys. Res.*, 86, 6673–6684.

Burlaga, L. F., S. P. Plunkett, and O. C. S. Cyr (2002), Successive CMEs and complex ejecta, *J. Geophys. Res.*, 107(A10), 1266, doi:10.1029/2001JA000255.

Burton, R. K., R. L. McPherron, and C. T. Russell (1975), An empirical relationship between interplanetary conditions and Dst, *J. Geophys. Res.*, 80, 4204–4214.

Chen, J. (1996), Theory of prominence eruption and propagation: Interplanetary consequence, *J. Geophys. Res.*, 101, 27,499–27,519.

Collier, M. R., R. P. Lepping, and D. B. Berdichevsky (2007), A statistical study of interplanetary shocks and pressure pulses internal to magnetic clouds, *J. Geophys. Res.*, 112, A06102, doi:10.1029/2006JA011714.

Dal Lago, A., et al. (2006), The 17–22 October (1999) solar-interplanetary-geomagnetic event: Very intense geomagnetic storm associated with a pressure balance between interplanetary coronal mass ejection and a high-speed stream, *J. Geophys. Res.*, 111, A07S14, doi:10.1029/2005JA011394.

Detman, T., Z. Smith, M. Dryer, C. D. Fry, C. N. Arge, and V. Pizzo (2006), A hybrid heliospheric modeling system: Background solar wind, *J. Geophys. Res.*, 111, A07102, doi:10.1029/2005JA011430.

Dryer, M., C. D. Fry, W. Sun, C. Deehr, Z. Smith, S.-I. Akasofu, and M. D. Andrews (2001), Prediction in real time of the 2000 July 14 heliospheric shock wave and its companions during the "Bastille" epoch, *Sol. Phys.*, 204, 267–286.

Dryer, M., Z. Smith, C. D. Fry, W. Sun, C. S. Deehr, and S.-I. Akasofu (2004), Real time shock arrival predictions during the "Halloween 2003 epoch," *Space Weather*, 2, S09001, doi:10.1029/2004SW000087.

Farrugia, C. J., and D. B. Berdichevsky (2004), Evolutionary signatures in complex ejecta and their driven shocks, *Ann. Geophys.*, 22, 3679–3698.

Farrugia, C. J., L. F. Burlaga, V. A. Osherovich, I. G. Richardson, M. P. Freeman, R. P. Lepping, and A. J. Lazarus (1993), A study of an expanding interplanetary magnetic cloud and its interaction with the Earth's magnetosphere: The interplanetary aspect, *J. Geophys. Res.*, 98, 7621–7632.

Farrugia, C. J., V. K. Jordanova, M. F. Thomsen, G. Lu, S. W. H. Cowley, and K. W. Ogilvie (2006), A two-ejecta event associated with a two-step geomagentic storm, *J. Geophys. Res.*, 111, A11104, doi:10.1029/2006JA011893.

Feng, X., and X. Zhao (2006), A new prediction method for the arrival time of interplanetary shocks, *Sol. Phys.*, 238, 167–186.

Fisher, G. (2004), Challenges facing the U.S. space weather public-private sector partnership, *Space Weather*, 2, S04003, doi:10.1029/2003SW000060.

Forbes, T. G., et al. (2006), CME theory and models, *Space Sci. Rev.*, 123, 251–302.

Fry, C. D., W. Sun, C. S. Deehr, M. Dryer, Z. Smith, S.-I. Akasofu, M. Tokumaru, and M. Kojima (2001), Improvements to the HAF solar wind model for space weather predictions, *J. Geophys. Res.*, 106, 20,985–21,001.

Fry, C. D., M. Dryer, W. Sun, C. S. Deehr, Z. Smith, T. R. Detman, A. Aran, D. Lario, B. Sanahuja, and S.-I. Akasofu (2005), Key links in space weather: Forecasting solar-generated shocks and proton acceleration, *AIAA. J.*, 43, 987–993.

Gonzalez, W. D., B. T. Tsurutani, and A. L. C. Gonzalez (1999), Interplanetary origin of geomagnetic storms, *Space Sci. Rev.*, 88, 529–562.

Gonzalez-Esparza, A., A. Santillan, and J. Ferrer (2004), A numerical study of the interaction between two ejecta in the interplanetary medium: One- and two-dimensional hydrodynamic simulations, *Ann. Geophys.*, 22, 3741–3749.

Gonzalez-Esparza, J. A. (2005), Numerical simulations of in situ observations of interacting ejecta near 1 AU, *Adv. Space Res.*, 35, 2162–2166.

Gopalswamy, N., A. Lara, R. P. Lepping, M. L. Kaiser, D. Berdichevsky, and O. C. S. Cyr (2000), Interplanetary acceleration of coroanl mass ejections, *Geophys. Res. Lett.*, 27, 145–148.

Gopalswamy, N., A. Lara, S. Yashiro, M. L. Kaiser, and R. A. Howard (2001a), Predicting the 1-AU arrival times of coronal mass ejections, *J. Geophys. Res.*, 106, 29,207–29,218.

Gopalswamy, N., S. Yashiro, M. L. Kaiser, R. A. Howard, and J. L. Bougeret (2001b), Radio signatures of coronal mass ejection interaction: coronal mass ejection cannibalism?, *Astrophys. J.*, 548, L91–L94.

Gosling, J. T., D. J. McComas, J. L. Phillips, and S. J. Bame (1991), Geomagnetic activity associated with Earth passage of interplanetary shock disturbances and coronal mass ejections, *J. Geophys. Res.*, 96, 7831–7839.

Groth, C. P. T., D. L. De Zeeuw, T. I. Gombosi, and K. G. Powell (2000), Global three-dimensional MHD simulation of a space weather event: CME formation, interplanetary propagation, and interaction with the magnetosphere, *J. Geophys. Res.*, 105, 25,053–25,078.

Hayashi, K., X. P. Zhao, and Y. Liu (2006), MHD simulation of two successive interplanetary disturbances driven by cone-model parameters in IPS-based solar wind, *Geophys. Res. Lett.*, 33, L20103, doi:10.1029/2006GL027408.

Hu, Y. Q., S. R. Habbal, Y. Chen, and X. Li (2003), Are coronal holes the only source of fast solar wind at solar minimum?, *J. Geophys. Res.*, 108(A10), 1377, doi:10.1029/2002JA009776.

Huttunen, K. E. J., R. Schwenn, V. Bothmer, and H. E. J. Koskinen (2005), Properties and geoeffectiveness of magnetic clouds in the rising, maximum and early declining phases of solar cycle 23, *Ann. Geophys.*, 23, 625–641.

Larson, D. E., R. P. Lin, J. M. McTiernan, J. P. McFadden, R. E. Ergun, M. McCarthy, H. Reme, T. R. Sanderson, M. Kaiser, R. P. Lepping, and J. Mazur (1997), Tracing the topology of the October 18–20 1995, magnetic cloud with $\sim 0.1 - 10^2$ keV electrons, *Geophys. Res. Lett.*, 24, 1911–1914.

Lugaz, N., W. B. Manchester IV, and T. I. Gombosi (2005), Numerical simulation of the interaction of two coronal mass ejections from Sun to Earth, *Astrophys. J.*, 634, 651–662.

Lugaz, N., W. B. Manchester IV, I. I. Roussev, G. Toth, and T. I. Gombosi (2007), Numerical investigation of the homologous CME events from active region 9236, *Astrophys. J.*, 659, 788–800.

Lundquist, S. (1950), Magnetohydrodynamic fields, *Ark. Fys*, 2, 361–365.

Manchester, W. B., T. I. Gombosi, I. Roussev, A. Ridley, D. L. De Zeeuw, I. V. Sokolov, K. G. Powell, and G. Toth (2004), Modeling a space weather event from the Sun to the Earth: CME generation and interplanetary propagation, *J. Geophys. Res.*, 109, A02107, doi:10.1029/2003JA010150.

McKenna-Lawlor, S. M. P., M. Dryer, M. D. Kartalev, Z. Smith, C. D. Fry, W. Sun, C. S. Deehr, K. Kecskemety, and K. Kudela (2006), Near real-

time predictions of the arrival at Earth of flare-related shocks during Solar Cycle 23, *J. Geophys. Res.*, *111*, A11103, doi:10.1029/2005JA011162.

Odstrcil, D., M. Vandas, V. J. Pizzo, and P. MacNeice (2003), Numerical simulation of interacting magnetic flux ropes, in *Solar Wind Ten*, edited by M. Velli, R. Bruno, and F. Malara, *AIP Conf. Proc.*, *679*, 699–702.

Odstrcil, D., P. Riley, and X. P. Zhao (2004a), Numerical simulation of the 12 May 1997 interplanetary CME event, *J. Geophys. Res.*, *109*, A02116, doi:10.1029/2003JA010135.

Odstrcil, D., V. J. Pizzo, J. A. Linker, P. Riley, R. Lionello, and Z. Mikic (2004b), Initial coupling of coronal and heliospheric numerical magnetohydrodynamic codes, *J. Atmos. Sol. Terr. Phys.*, *66*, 1311–1320.

Odstrcil, D., V. J. Pizzo, and C. N. Arge (2005), Propagation of the 12 May 1997 interplanetary coronal mass ejection in evolving solar wind structures, *J. Geophys. Res.*, *110*, A02106, doi:10.1029/2004JA010745.

Owens, M. J., V. J. Merkin, and P. Riley (2006), A kinematically distorted flux rope model for magnetic clouds, *J. Geophys. Res.*, *111*, A03104, doi:10.1029/2005JA011460.

Richardson, I. G., and H. V. Cane (2004), The fraction of interplanetary coronal mass ejections that are magnetic clouds: Evidence for a solar cycle variation, *Geophys. Res. Lett.*, *31*, L18804, doi:10.1029/2004GL020958.

Richardson, I. G., and H. V. Cane (2005), A survey of interplanetary coronal mass ejections in the near-Earth solar wind during 1996–2005, in *Solar Wind 11*, edited by B. Fleck et al., *Eur. Space Agency Spec. Publ.*, ESA SP-592, 755.

Schmidt, J. M., and P. J. Cargill (2003), Magnetic reconnection between a magnetic cloud and the solar wind magnetic field, *J. Geophys. Res.*, *108*(A1), 1023, doi:10.1029/2002JA009325.

Schmidt, J. M., and P. J. Cargill (2004), A numerical study of two interacting coronal mass ejections, *Ann. Geophys.*, *22*, 2245–2254.

Shen, F., X. Feng, S. T. Wu, and C. Xiang (2007), Three-dimensional MHD simulation of CMEs in three-dimensional background solar wind with the self-consistent structure on the source surface as input: Numerical simulation of the January 1997 Sun-Earth connection event, *J. Geophys. Res.*, *112*, A06109, doi:10.1029/2006JA012164.

Smart, D. F., and M. A. Shea (1985), A simplified model for timing the arrival of solar flare-initiated shocks, *J. Geophys. Res.*, *90*, 183–190.

Smith, Z., and M. Dryer (1990), MHD study of temporal and spatial evolution of simulated interplanetary shocks in the ecliptic plane within 1 AU, *Sol. Phys.*, *129*, 387–405.

Toth, G., et al. (2005), Space Weather Modeling Framework: A new tool for the space science commnunity, *J. Geophys. Res.*, *110*, A12226, doi:10.1029/2005JA011126.

Tsurutani, B. T., W. D. Gonzalez, F. Tang, S.-I. Akasofu, and E. J. Smith (1988), Origin of interplanetary southward magnetic fields responsible for major magnetic storms near solar maximum (1978–1979), *J. Geophys. Res.*, *93*, 8519–8531.

Vandas, M., S. Fischer, M. Dryer, Z. Smith, and T. Detman (1995), Simulation of magnetic cloud propagation in the inner heliosphere in two dimensions: 1. A loop perpendicular to the ecliptic plane, *J. Geophys. Res.*, *100*, 12,285–12,292.

Vandas, M., S. Fischer, M. Dryer, Z. Smith, and T. Detman (1996), Simulation of magnetic cloud propagation in the inner heliosphere in two dimensions: 2. A loop parrallel to the ecliptic plane and the role of helicity, *J. Geophys. Res.*, *101*, 2505–2510.

Vandas, M., S. Fischer, M. Dryer, Z. Smith, T. Detman, and A. Geranios (1997), MHD simulation of an interaction of a shock wave with a magnetic cloud, *J. Geophys. Res.*, *102*, 22,295–22,300.

Vandas, M., D. Odstrcil, and S. Watari (2002), Three-dimensional MHD simulation of a loop-like magnetic cloud in the solar wind, *J. Geophys. Res.*, *107*(A9), 1236, doi:10.1029/2001JA005068.

Wang, A. H., S. T. Wu, and N. Gopalswamy (2005), Magnetohydrodynamic analysis of January 20, 2001, CME-CME interaction event, in *Particle Acceleration in Astrophysical Plasmas: Geospace and Beyond*, *Geophys. Monogr. Ser.*, vol. 156, edited by D. Gallagher et al., pp. 185–195, AGU, Washington, D. C.

Wang, Y. M. (2003), Comprehensive studies on magnetic clouds in interplanetay space and their associated events, Ph.D. thesis, Univ. of Sci. and Technol. of China, Anhui, China.

Wang, Y. M., S. Wang, and P. Z. Ye (2002), Multiple magnetic clouds in interplanetary space, *Sol. Phys.*, *211*, 333–344.

Wang, Y. M., S. Wang, and P. Z. Ye (2003a), Multiple magnetic clouds: Several examples during March–April, 2001, *J. Geophys. Res.*, *108*(A10), 1370, doi:10.1029/2003JA009850.

Wang, Y. M., P. Z. Ye, S. Wang, and X. H. Xue (2003b), An interplanetary cause of large geomagnetic storms: Fast forward shock overtaking preceding magnetic cloud, *Geophys. Res. Lett.*, *30*(13), 1700, doi:10.1029/2002GL016861.

Wang, Y. M., C. L. Shen, S. Wang, and P. Z. Ye (2003c), An impirical formula relating the geomagnetic storm's intensity to the interplanetary

parameters: $-\overline{VB_z}$ and Δt, *Geophys. Res. Lett.*, *30*(20), 2039, doi:10.1029/2003GL017901.

Wang, Y. M., P. Z. Ye, S. Wang, and M. Xiong (2003d), Theoretical analysis on the geoeffectiveness of a shock overtaking a preceding magnetic cloud, *Solar Phys.*, *216*, 295–310.

Wang, Y. M., P. Z. Ye, S. Wang, and H. N. Zheng (2004) MHD simulation of the propagtion and evolution of multiple magnetic clouds in the heliosphere, paper presented at 35th Scientific Assembly, COSPAR, Paris, France.

Wang, Y. M., H. N. Zheng, S. Wang, and P. Z. Ye (2005), MHD simulation of formation and propagation of multiple magnetic clouds in the heliosphere, *Astron. Astrophys.*, *434*, 309–316.

Wei, F. S., R. Liu, Q. Fan, and X. Feng (2003a), Identification of the magnetic cloud boundary layers, *J. Geophys. Res.*, *108*(A6), 1263, doi:10.1029/2002JA009511.

Wei, F. S., R. Liu, X. Feng, D. Zhong, and F. Yang (2003b), Magnetic structures inside boundary layers of magnetic clouds, *Geophys. Res. Lett.*, *30*(24), 2283, doi:10.1029/2003GL018116.

Wei, F. S., X. Feng, F. Yang, and D. Zhong (2006), A new non-pressure-balanced structure in interplanetary space: Boundary layers of magnetic clouds, *J. Geophys. Res.*, *111*, A03102, doi:10.1029/2005JA011272.

Wu, C.-C., and R. P. Lepping (2002a), Effect of solar wind velocity on magnetic cloud-associated magnetic storm intensity, *J. Geophys. Res.*, *107*(A11), 1346, doi:10.1029/2002JA009396.

Wu, C.-C., and R. P. Lepping (2002b), Effects of magnetic clouds on the occurrence of geomagnetic storms: The first 4 years of Wind, *J. Geophys. Res.*, *107*(A10), 1314, doi:10.1029/2001JA000161.

Wu, C.-C., R. P. Lepping, and N. Gopalswamy (2003), Variations of magnetic clouds and CMEs with solar activity cycle, in *Proceedings of ISCS 2003 Symposium, "Solar Variability as an Input to the Earth's Environment,"* edited by A. Wilson, *Eur. Space Agency Spec. Publ.*, ESA SP-535, 429–432.

Wu, C.-C., S. T. Wu, and M. Dryer (2004a), Evolution of fast and slow shock interactions in the inner heliosphere, *Sol. Phys.*, *223*, 259–282.

Wu, C.-C., M. Dryer, and S. T. Wu (2004b), Temporal evolution of slow shock interactions in the solar wind, paper presented at 35th Scientific Assembly, COSPAR, Paris, France.

Wu, C.-C., C. D. Fry, D. Berdichevsky, M. Dryer, Z. Smith, and T. Detman (2005a), Predicting the arrival time of shock passages at Earth, *Sol. Phys.*, *227*, 371–386.

Wu, C.-C., C. D. Fry, B. J. Thompson, S. T. Wu, M. Dryer, and K. Liou (2005b), Three-dimensional global simulation of CME/ICME/Shock propagation from Sun to the heliosphere, *Eos Trans. AGU*, *86*(52), Fall Meet. Suppl., Abstract SH14A–03.

Wu, C. C., et al. (2005c), Flare-generated shock evolution and geomagnetic storms during the "Halloween 2003 epoch": 29 October to 2 November, *J. Geophys. Res.*, *110*, A09S17, doi:10.1029/2005JA011011.

Wu, C.-C., R. P. Lepping, and N. Gopalswamy (2006a), Relationships among magnetic clouds, CMEs, and geomagnetic storms, *Sol. Phys.*, *239*, 449–460.

Wu, C.-C., C. Fry, S. T. Wu, M. Dryer, B. Thompson, K. Liou, and X. S. Feng (2006b), The evolution and interaction of multiple coronal mass ejections, paper presented at 36th Scientific Assembly, COSPAR, Beijing, China.

Wu, C.-C., X. S. Feng, S. T. Wu, M. Dryer, and C. D. Fry (2006c), Effects of the interaction and evolution of interplanetary shocks on "background" solar wind speeds, *J. Geophys. Res.*, *111*, A12104, doi:10.1029/2006JA011615.

Wu, C.-C., S. Wu, M. Dryer, C. Fry, D. Berdichevsky, Z. Smith, and T. Detman (2007a), The evolution of shocks near the surface of Sun during the epoch of Halloween 2003, *J. Atmos. Terr. Phys.*, *69*, 91–100.

Wu, C.-C., C. D. Fry, S. T. Wu, M. Dryer, and K. Liou (2007b), Three-dimensional global simulation of interplanetary coronal mass ejection propagation from Sun to the heliosphere: Solar event of 12 May 1997, *J. Geophys. Res.*, *112*, A09104, doi:10.1029/2006JA012211.

Wu, C.-C., C. Fry, M. Dryer, S. Wu, B. Thompson, K. Liou, and X. Feng (2007c), Three-dimensional global simulation of multiple ICMEs' interaction and propagation from the Sun to the heliosphere following the 25–28 October 2003 solar events, *Adv. Space Res.*, in press.

Wu, S. T., A. H. Wang, and D. A. Falconer (2005), A three-dimensional magnetohydrodynamic (MHD) model of active region evolution, in *Coronal and Stellar Mass Ejection, IAU Symposium Proceedings of the International Astronomical Union 226, 13–17 September, Beijing*, edited by K. Dere, J. Wang, and Y. Yan, pp. 291–301, Cambridge Univ. Press, Cambridge, UK.

Wu, S. T., A. H. Wang, Y. Liu, and J. T. Hoeksema (2006), Data-driven magnetohydrodynamic model for active region evolution, *Astrophys. J.*, *652*, 800–811.

Xie, H., N. Gopalswamy, P. K. Manoharan, A. Lara, S. Yashiro, and S. Lepri (2006), Long-lived geomagnetic storms and coronal mass ejections, *J. Geophys. Res.*, *111*, A01103, doi:10.1029/2005JA011287.

Xiong, M., H. N. Zheng, Y. M. Wang, X. R. Fu, S. Wang, and X. K. Dou (2005), A numerical simulation on the solar-terrestrial transit time of successive CMEs during November 4–5, 1998, *Chin. J. Geophys.*, *48*, 805–813.

Xiong, M., H. N. Zheng, Y. M. Wang, and S. Wang (2006a), Magnetohydrodynamic simulation of the interaction between interplanetary strong shock and magnetic cloud and its consequent geoeffectiveness, *J. Geophys. Res.*, *111*, A08105, doi:10.1029/2005JA011593.

Xiong, M., H. N. Zheng, Y. M. Wang, and S. Wang (2006b), Magnetohydrodynamic simulation of the interaction between interplanetary strong shock and magnetic cloud and its consequent geoeffectiveness: 2. Oblique collision, *J. Geophys. Res.*, *111*, A11102, doi:10.1029/2006JA011901.

Xue, X. H., Y. M. Wang, P. Z. Ye, S. Wang, and M. Xiong (2005), Analysis on the interplanetary causes of the great magnetic storms in solar maximum (2000–2001), *Planet. Space Sci.*, *53*, 443–457.

Zhang, J., et al. (2007), Solar and interplanetary sources of major geomagnetic storms ($Dst \leq -100$ nT) during 1996–2005, *J. Geophys. Res.*, *112*, A10102, doi:10.1029/2007JA012321.

———————————

S. Wang, Y. Wang, M. Xiong, and H. Zheng, School of Earth and Space Sciences, University of Science and Technology of China, Hefei, Anhui 230026, China. (swan@ustc.edu.cn; ymwang@ustc.edu.cn; mxiong@ustc.edu.cn; hue@ustc.edu.cn)

S. T. Wu, Center for Space Plasma and Aeronomic Research, University of Alabama in Huntsville, Huntsville, AL 35899, USA. (wus@cspar.uah.edu)